AGU ADVANCING EARTH AND SPACE SCIENCES

Earth's Future

Key Points:

- Stratospheric Aerosol Injections do not fully compensate for atmospheric circulation changes from climate change but create new dynamics
- Total global wind energy potential is negligibly reduced under Stratospheric Aerosol Injections but regional trends tend to vary substantially
- Results are based on hourly output from CNRM-ESM2-1. Changes are likely to be larger in other GeoMIP models in the northern hemisphere

Change in Wind Renewable Energy Potential Under Stratospheric Aerosol Injections

Susanne Baur[1] [ID]**, Benjamin M. Sanderson[2], Roland Séférian[3]** [ID]**, and Laurent Terray[1]** [ID]

[1]CECI, Université de Toulouse, CERFACS, CNRS, Toulouse, France, [2]Centre for International Climate and Environmental Research (CICERO), Oslo, Norway, [3]CNRM, Université de Toulouse, Météo-France/CNRS, Toulouse, France

Abstract Wind renewable energy (WRE) is an essential component of the global sustainable energy portfolio. Recently, there has been increasing discussion on the potential supplementation of this conventional mitigation portfolio with Solar Radiation Modification (SRM). However, the impact of SRM on conventional mitigation measures has received limited attention to date. In this study, we explore one part of this impact, the potential effect of one type of SRM, Stratospheric Aerosol Injections (SAI), on WRE. Using hourly output from the Earth System Model CNRM-ESM2-1, we compare WRE potential under a medium emission scenario (SSP245) and a high emission scenario (SSP585) with an SRM scenario that has SSP585 baseline conditions and uses SAI to offset warming to approximately SSP245 global warming levels. Our results suggest that SAI may affect surface wind resources by modifying large-scale circulation patterns, such as a significant poleward jet-shift in the Southern Hemisphere. The modeled total global WRE potential is negligibly reduced under SAI compared to the SSP-scenarios. However, regional trends are highly variable, with large increases and decreases in WRE potential frequently reaching 12% across the globe with SAI. This study highlights potential downstream effects of SRM on climatic elements, such as wind patterns, and offers perspectives on its implications for our mitigation efforts.

Plain Language Summary Wind renewable energy (WRE) is a pivotal element of the global transition toward sustainable energy. Recently, there has been a surge of interest in Solar Radiation Modification (SRM) as a potential means of managing climate impacts, but its effects on existing strategies like WRE have not been much addressed in the current literature. This research examines the potential impact of one type of SRM, Stratospheric Aerosol Injections (SAI), on WRE potential. An Earth System Model is used to compare WRE potential under three climate scenarios: one with moderate emissions, one with high emissions and one where SAI is used to reduce warming in the high-emission scenario to match the moderate-emission global warming level. The findings suggest that SAI may result in a minimal reduction in long-term global mean WRE potential. However, the effects vary considerably by region and season, with areas experiencing changes in WRE potential that frequently reach approximately 12%. This research highlights the potential for SAI to exert complex effects on wind patterns, which could influence the future of renewable energy strategies.

1. Introduction

Wind renewable energy (WRE) is a key component of the transition to a low-carbon energy system (Clarke et al., 2022; IPCC, 2018; Riahi et al., 2022). Modeling assessments estimate that in Paris Agreement compatible scenarios, such as the C1 and C2 scenarios from the recent IPCC Assessment Report (Riahi et al., 2022), a substantial portion of energy would come from wind with projected production ranging from 4,760 to 50,960 TWh/yr by 2050 depending on the scenario and model (Byers et al., 2022). However, present policies are taking us closer to a global mean surface temperature increase of 2.5–2.9°C than the Paris compatible 1.5°C (CAT, 2023), whilst current warming already leads to numerous climate change related damages (Ripple et al., 2023). Hence, there is growing interest in a group of technologies, termed Solar Radiation Modification (SRM) (Climate Overshoot Commission, 2023), as a potential addition to conventional mitigation, to rapidly manage climate change risks. SRM does not resolve the global warming problem as it does not eliminate greenhouse gases (GHGs), but is proposed to temporarily mask some of the impacts with the logic of providing more time to sufficiently roll out mitigation measures and halt or reverse the rise of atmospheric GHG concentration (Horton, 2015; MacCracken, 2009; Royal Society, 2011; Schäfer et al., 2014). It works by modifying the balance of incoming and outgoing radiation in the Earth system, which, if done on a significant scale, can exert a global cooling effect to counteract warming due to greenhouse gases. SRM is perceived controversially by

experts and laypeople alike (Müller-Hansen et al., 2023) due, in part, to the large social and ecological risks and unknowns involved in intentionally manipulating the complex Earth system.

Various proposals have been put forward to alter the radiative equilibrium, with the injection of aerosols into the stratosphere (SAI) receiving the most attention thus far. An initial proposed strategy of SAI intervention aiming at global impact entails the continuous placement of aerosols at low latitudes in the lower stratosphere (Dai et al., 2018; Kravitz et al., 2019; Tilmes, Richter, Mills et al., 2018b; Tilmes et al., 2017), where the Brewer-Dobson circulation slowly transports them toward the poles. The aerosols reflect the incoming short-wave radiation allowing less radiative energy to reach the surface. While this process leads to cooling at the surface, evidenced by large volcanic eruptions, not all radiation is reflected by the aerosols. Instead, some of the radiative energy is absorbed by the particles, leading to localized heating of the stratosphere, which can affect global circulation patterns (Baldwin & Dunkerton, 2001; DallaSanta et al., 2019; Graft et al., 1993; Stenchikov et al., 2002). For example, several studies on the impact of stratospheric aerosols from volcanic eruptions have found a poleward jet shift (Barnes et al., 2016; Polvani & Kushner, 2002; Simpson et al., 2009). This has been attributed to two general mechanisms, surface cooling and stratospheric warming (DallaSanta et al., 2019). The surface cooling from the stratospheric aerosols decreases the tropospheric meridional temperature gradient (Graf, 1992; Stenchikov et al., 2002), which reduces midlatitude baroclinity, driving a strengthening of the stratospheric vortex, which leads to a poleward shift of the jet (Baldwin & Dunkerton, 2001). The second and primary mechanism, however, is the observed warming of the stratosphere in the tropics due to the aerosol's absorption of the radiative energy. This enhances the stratospheric meridional temperature gradient leading to a strengthened stratospheric vortex that shifts the jet poleward (DallaSanta et al., 2019). While observations from volcanic aerosols are not necessarily indicative of potential modifications under SAI, modeling studies on SAI impacts have also found large-scale circulation changes. Liu et al. (2023) studied the East Asian Winter Monsoon under SAI and found that aerosol injections reverse the weakening of the monsoon that occurs in SSP585. In Africa, however, SAI can lead to weaker monsoon winds (Da-Allada et al., 2020; Robock et al., 2008) and a slight southward shift of the ITCZ (Cheng et al., 2019). It should be emphasized that the outcomes of these studies are likely strongly reliant on the selected injection design and the underlying model (Kravitz et al., 2016; H. Lee et al., 2020; MacMartin & Kravitz, 2019).

Wind power generation relies significantly on local and regional wind patterns and even minor fluctuations in wind velocity can have a meaningful impact on the energy output (Veers et al., 2019). This is because the energy in the wind follows the cube of the wind speed. While to our knowledge no research has been conducted on WRE potential under SRM, several studies have looked at the impact of climate change in general on wind potential. They found significant alterations in wind velocity and its temporal distribution as a result of global warming (Solaun & Cerdá, 2019). One of the main mechanisms behind large-scale circulation changes from anthropogenic warming is the reduced equator-to-pole temperature gradient at the surface as a result from polar amplification, which is expected to alter tropical circulation (Ma et al., 2012), such as the Hadley cell, monsoon circulations and tropical cyclone frequency, as well as the behavior of midlatitude jet streams and storm tracks (Martinez & Iglesias, 2024; Pryor et al., 2020; Shaw et al., 2016). However, wind resources can be further impacted by ocean circulation and surface roughness changes from land cover modifications (Jung & Schindler, 2022; Vautard et al., 2010; Zeng et al., 2019). Additionally, local wind resources exhibit high variability on sub-hourly and multi-decadal scales (Jung et al., 2018). Due to the difficulty to accurately represent all drivers and the resulting temporal and spatial variations of wind patterns in Global Circulation Models, it is not entirely certain whether climate change will result in a decrease or increase in wind speeds at the global scale (Pryor et al., 2020). Most studies find highly diverse regional trends with large increases and decreases in wind speed and wind energy potential all over the globe (Gernaat et al., 2021; Jung & Schindler, 2022; Pryor et al., 2020; Solaun & Cerdá, 2019). As a result, on a global scale, changes in total wind energy density (Martinez & Iglesias, 2024) and wind energy potential (Gernaat et al., 2021) are small and may be slightly negative.

Given that WRE already plays an important role in the prevailing mitigation strategy, and that mitigation is an important aspect of ensuring the temporary use of SRM, it is important to understand whether SRM complements or conflicts with this existing method of energy generation and mitigation. Only through an understanding of the full spectrum of consequences from SAI can responsible decision-making be enabled. Here, we analyze the interplay between WRE and SAI by calculating and comparing on- and offshore wind potential when one of the proposed deployments of SAI is used versus when mitigation has brought the climate to approximately the same

GMST (SSP245). Additionally, we compare the SAI-modified climate with the fossil-fuel heavy emission baseline of the scenario without SAI (SSP585).

2. Model Experiments and Methods

2.1. Data and Simulations

This study is based on three experiments: a fossil-fuel intensive, high-emission scenario called SSP585 (O'Neill et al., 2016), a moderately ambitiously mitigated scenario, SSP245 (O'Neill et al., 2016), and a stratospheric aerosol injection (SAI) simulation that cools down from an SSP585 baseline to SSP245 (see Figure S1 in Supporting Information S1 for an illustration of the global mean temperature evolution of each scenario). The SAI experiment originates from the Geoengineering Model Intercomparison Project GeoMIP6 protocol (Kravitz et al., 2015) and is referred to therein as G6sulfur. We run these experiments from 2015 to 2100 in a 6-member ensemble with perturbed initial conditions on the CNRM-ESM2-1 Earth System Model (Séférian et al., 2019). Due to the unavailability of necessary high-frequency output from other Earth System Models participating in GeoMIP, only one model is used. However, CNRM-ESM2-1 performs well compared to other Earth System Models of the same generation (CMIP6) in terms of lower and upper troposphere zonal wind (Text S1, Figures S2–S4 in Supporting Information S1). See Texts S1, S2 and Table S4 in Supporting Information S1 for more details on CNRM-ESM2-1's performance compared to other CMIP6 and GeoMIP models. Ensemble means are displayed except if defined otherwise. Value ranges indicated in brackets in the text refer to the 95% confidence intervals. As a proxy for SAI we use prescribed 2D monthly aerosol optical depth derived from the GeoMIP G4SSA experiment (Tilmes et al., 2015) which scales up to 0.35 in the last decade of the simulation. The variables related to the directional winds u and v at 150 m altitude are produced at hourly resolution on a $1° \times 1°$ grid. During the postprocessing we bilinearly regrid the climate model output to match the land use and land cover data (described in Section 2.2.3 Politico-economic dimension) which is on a $0.1° \times 0.1°$ grid. For the zonal winds we create two altitudinal categories: upper and surface. Upper refers to a pressure level of 200–400 hPa, roughly corresponding to the upper troposphere, and surface, referring to a pressure level of 850–1,050 hPa, representing the air close to the Earth's surface.

2.2. Wind Potential Calculation

In the same manner as Baur et al. (2024), we use the term "potential" to refer to an enhanced version of the traditional definition of the "technical potential." The technical potential is the theoretical potential, here the surface wind resource, constrained by geographical and technical restrictions. In this study, we distinguish between three dimensions that are involved in the wind energy potential calculation: the technical dimension that establishes the technical restrictions to the theoretical potential, the physical dimension, which is related to the energy extractable from surface wind speed, and the politico-economic one, which is related to the suitability of the grid cell i for wind turbine placement. We calculate the wind potential in a similar fashion to Gernaat et al. (2021) as:

$$TP_{i,loc} = Politicoeconomic_i \times Technical_{loc} \times Physical_{i,loc} \times gridcell_i \left[\frac{MWh}{yr}\right] \quad (1)$$

All parameters, their values, units and sources are given in Table S1 in Supporting Information S1. The subscript *loc* indicates whether it is an on- or offshore wind farm. The resulting electricity generation potential is expressed in various time slices, such as 10-year seasonal mean changes, weekly sums and yearly sums, calculated from the hourly wind speed input. Seasons refer to the four periods DJF (December, January, February), MAM (March, April, May), JJA (June, July, August) and SON (September, October, November). We calculate the Low Energy Week (LEW) metric as introduced by Baur et al. (2024).

2.2.1. Technical Dimension

This part of the calculation reduces the physical potential by accounting for the unavailability of the turbines due to maintenance, the wind farm array inefficiencies and the density of wind turbine placement. We use technical indicators from on- and offshore representative real-world wind turbines. To avoid projecting technological developments into the future we choose turbines which are either already or about to be in serial production but

are at the forefront of current wind turbine development. We justify this choice with the argument that the average wind turbines of the future will be the most powerful wind turbines of today. Table S2 in Supporting Information S1 lists their characteristics.

The technical dimension consists of η_a, the annual availability of the turbine due to maintenance, η_{ar}, the wind farm array efficiency, and D_{loc}, the turbine density, and is a simple multiplication of these terms:

$$\text{Technical}_{\text{loc}} = \eta_{\text{a}} \times \eta_{\text{ar}} \times D_{loc} \left[\frac{\text{turbines}}{\text{km}^2} \right] \qquad (2)$$

D is the average installed turbine density in the grid cell and is calculated as:

$$D_{loc} = \frac{1}{(\text{spacing} \times d_{\text{Rotor},loc})^2} \left[\frac{\text{turbines}}{\text{km}^2} \right] \qquad (3)$$

We assume that turbine spacing is equal in prevailing and perpendicular wind direction. For the turbines set out in Table S2 in Supporting Information S1, this gives a D_{onshore} of 1.56 turbines/km² and a D_{offshore} of 0.51 turbines/km². Translated into the more commonly used metric power density, this implies 9.68 MW/km² onshore and 7.65 MW/km² offshore.

2.2.2. Physical Dimension

The physical dimension represents the power produced by a wind turbine $p(v)$, which is described by the wind turbine power curve (Carrillo et al., 2013; Saint-Drenan et al., 2020; Figure S5 in Supporting Information S1) and calculated as:

$$p(v_i)_i = \begin{cases} 0 & v < v_{ci} \ or \ v > v_{co} \\ q(v_i) & v_{ci} \leq v < v_r \\ P_r & v_r \leq v \leq v_{co} \end{cases} \qquad (4)$$

The power curve depends on the instantaneous wind speed v and the characteristics of the wind turbine (Table S2 in Supporting Information S1) and distinguishes between four different operation regimes (Figure S5 in Supporting Information S1): I, the area of wind speeds (v) that are smaller than the cut-in wind speed (v_{ci}), and therefore too low to produce any energy, II, the area of non-linear relationship between wind speed and power output ($q(v)$), III, the area of maximum power output, that is, rated power (P_r), and IV, the area after the cut-out threshold, where wind speed is too high ($v > v_{co}$) and turbines shut down to protect themselves from damage (Saint-Drenan et al., 2020; Wood & Wollenberg, 1996).

Power production in area II follows the parametric wind turbine power curve described in Saint-Drenan et al. (2020) and is calculated as:

$$q(v_i) = 0.5 \times \rho \times \varepsilon_{loc} \times v^3 \times \text{pc} \left[\frac{\text{MWh}}{\text{turbine}} \right] \qquad (5)$$

With ρ being the air density, which is kept constant, ε the area swept by the rotor blades calculated from the rotor blade diameters (Table S2 in Supporting Information S1), v instantaneous wind speed and pc the power coefficient, a measure for aerodynamic-mechanical-electrical performance of the turbines (Veers et al., 2019). For simplicity, in our study, the power coefficient is held constant, however, as demonstrated in Saint-Drenan et al. (2020), it is ultimately dependent on and varies with the wind's velocity. The power coefficient parameterization leads to a slight overestimation in power output from higher wind speeds and underestimation of output from lower wind speeds in the $q(v_i)$-part of our calculation.

Due to the high variability of wind, a temporal resolution of 1 hr and a spatial resolution of 1° × 1° may not adequately represent all prevailing wind speeds in the area during the specified time period. To account for the requirement of instantaneous wind velocity in the wind power curve calculation and the low spatial resolution of

the input data, we represent wind speed through a probability density function. Weibull distributions have frequently been used to represent the spread in wind speed over a time period at a given location (e.g., Aukitino et al., 2017; Mohammadi et al., 2016; Shi et al., 2021; Shu et al., 2015) and as a means of downscaling to represent the spread of wind over a larger area (Alizadeh et al., 2020; Chang et al., 2015; Tye et al., 2014; Zhou & Smith, 2013). The temporal resolution of the underlying wind data can range from 10 min (Eskin et al., 2008), to hourly (Burton et al., 2001; Chang et al., 2015; Li et al., 2020; Mohammadi et al., 2016), 6-hourly (Elsner, 2019), to daily (Shu & Jesson, 2021) and longer. Cradden et al. (2014) and Pryor et al. (2020) have highlighted the importance of a high temporal resolution of at least 1 hr for WRE analyses. Although hourly and daily average wind speeds have been shown to lead to similar power output results from a turbine over a long time period, hourly input data is much better at representing the peaks and lows during the day and can give a more precise result for shorter time periods (Justus et al., 1978; Shin et al., 2018; Veronesi & Grassi, 2015). In this study, the Weibull distribution is used to represent sub-grid spatial and temporal variation in wind. We use a constant shape-parameter for all regions across the globe. This is a frequently applied simplification (Arent et al., 2012; Dvorak et al., 2010; Elsner, 2019; Eurek et al., 2017; Shu et al., 2015; Sohoni et al., 2016; Valencia Ochoa et al., 2019) related to the width of the distribution and therefore the gustiness of the wind regimes (Eurek et al., 2017) that is most commonly used in larger scale analyses. Studies have demonstrated variation of the shape parameter across regions (Zhou & Smith, 2013), especially for oceanic winds (Perrin et al., 2006; Shi et al., 2021). However, apart from coastal areas, oceanic regions are excluded from this analysis and using the Rayleigh-form of the Weibull distribution, which sets the shape parameter β to 2 and implies moderately gusty winds across all areas (Eurek et al., 2017), drastically reduces the computational effort. The scale parameter, α, is calculated according to Lysen (1983) as follows:

$$\alpha = ws_i \times (0.568 + 0.433 \times 0.5)^{\frac{1}{\beta}} \tag{6}$$

with ws_i being the hourly wind speed from our model output calculated as the square root of the sum of the squares of the east- and northward wind components u and v. We calculate $p(v)$ for all 1,000 samples in the Weibull distribution for each 1 m/s wind speed bin from 0 to 50 m/s.

The 2-parameter Weibull distribution representing the range of wind speeds prevalent in the 1-hr mean 1° grid cell model output is calculated as:

$$f(T) = \frac{\beta}{\alpha} \times \left(\frac{T}{\alpha}\right)^{\beta-1} \times e^{-\left(\frac{T}{\alpha}\right)^{\beta}} \tag{7}$$

For computational feasibility we fit a curve between the 1-hr mean wind speed and the power output, that is, $p(v)$, that takes into account the Weibull spread of wind speed and the turbine power curve:

$$\text{Physical}_{i,loc} = p(ws_i)_{loc} = a_{loc} \times \left(1 - e^{\frac{-ws_i^2}{b_{loc}}}\right) \times \left(1 - e^{\frac{-ws_i^2}{c_{loc}}}\right) \times e^{\frac{-ws_i}{d_{loc}}} \left[\frac{MWh}{\text{turbine}}\right] \tag{8}$$

Please consult Table S1 in Supporting Information S1 for the values of the parameters a_{loc}, b_{loc}, c_{loc}, and d_{loc}. To assess how much energy is lost due to a change in the distribution of hourly wind speeds we additionally calculate the wind potential without the cut-out wind speed limit (no-cut-out). Instead, power output at $v > v_{co}$ is kept at P_r. By subtracting the yearly cumulative "standard"-turbine-power-curve power output with the output from these no-cut-out calculations, we can estimate the amount of TWh that is gained or lost in a year due to a change in fast winds. Figure S6 in Supporting Information S1 shows the fitted power curve of an onshore and offshore grid cell in the normal setting and in the no-cut-out-setting.

2.2.3. Politico-Economic Dimension

The incorporation of a politico-economic dimension is a long-standing approach for wind potential calculations (e.g., Archer & Jacobson, 2005; Bosch et al., 2017; Elliot & Schwartz, 1993; Hoogwijk, 2004; Zhou et al., 2012) and is related to the suitability of each grid cell to harbor wind turbines. Various parameters have been taken into
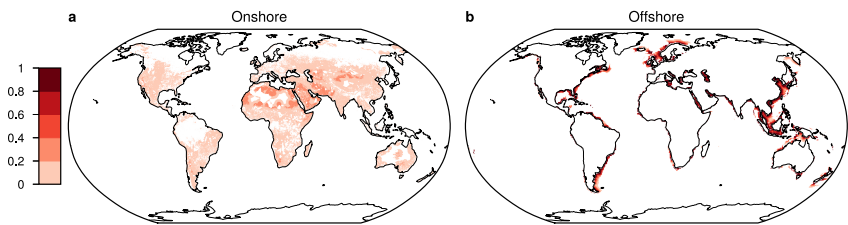
Figure 1. Combined masking effect of the single area restrictions for (a) onshore and (b) offshore.

account in the past. Here, we consider surface properties and land use competition for our onshore wind farms as done in Baur et al. (2024).

Figure 1 displays the combined masking effect of the single area restrictions for on- and offshore wind farms which are used in the wind potential calculation (Politicoeconomic$_i$). The single area restrictions and their weights are displayed in Figures S7 and S8 in Supporting Information S1. We exclude all areas marked as protected with any status as characterized by the United Nations Environment Program (IUCN, 2023) as possible wind power installation sites and weigh areas according to the prevalent land-use and distance to highly populated centers as an indicator for the future existence of transmission lines and demand. Highly populated areas are excluded since wind turbines are rarely situated in close proximity to, or on top of, buildings. For offshore we add additional constraints, such as the bathymetry over 1000 m, exclusion of grid cells outside the Exclusive Economic Zone (EEZ) (Flanders Marine Institute, 2019) and consideration of only those grid cells that are at least 95% sea-ice free in every season of the year.

Land-use cover and population density data were obtained from the IMAGE3.0-LPJ model (Doelman et al., 2018; Stehfest et al., 2014) with a spatial resolution of $0.1° \times 0.1°$. The model differentiates between 20 different land use and land cover categories. We weigh each type according to the fraction of a grid cell that could be covered by wind farms, in line with Baur et al. (2024), but with different fractions assigned (see Table S3 in Supporting Information S1 for land use categories and assigned suitability fractions). The rationale behind the suitability fraction is that only part of a grid cell is available for wind farms as they could potentially conflict with other land uses such as cities, agricultural production or ecosystem services from forests. A suitability fraction of 15% denotes that 15% of the grid cell is able to accommodate a wind farm. The spacing between the turbines of several hundred meters enables a certain level of coexistence between wind farms and predominant land uses. This explains the assignment of higher fractions for, for example, agricultural areas in this study than in Baur et al. (2024), which looked at solar farms.

We use the same approach as Baur et al. (2024) to weigh the proximity to highly populated areas. The population data from the IMAGE3.0 LPJ model consists of 5-year intervals and is aggregated to 10-year means for our analysis (Doelman et al., 2018; Stehfest et al., 2014). Using a sigmoidal function, we impose that the weight diminishes proportionally as the distance to densely populated cells grows, ultimately tapering to zero at approximately 500 km. Unlike Baur et al. (2024), we exclude highly populated areas, which we define as cells where population density is larger than 1,000 inhabitants/km^2.

We present results that are calculated using equal weights across all scenarios and time intervals. Therefore, the data underlying population, sea ice and land use are related to the 2090–2099 time frame of SSP245 but are used as a basis for all three scenarios. Total suitable land area varies minimally between the scenarios and does not impact the main result.

3. Results

3.1. Large-Scale Circulation Response to SAI

Our simulations indicate substantial alterations in 10-year mean zonal wind from the present (2015–2024) to the end of the century (2090–2099) (Figure S9 in Supporting Information S1). While the patterns of change show some similarities for SAI, SSP585 and SSP245, the magnitude of the circulation differences from present to future varies considerably and is especially pronounced for SAI and SSP585 (Figure S9 in Supporting Information S1). When comparing the future conditions of the scenarios with each other, substantial differences become apparent
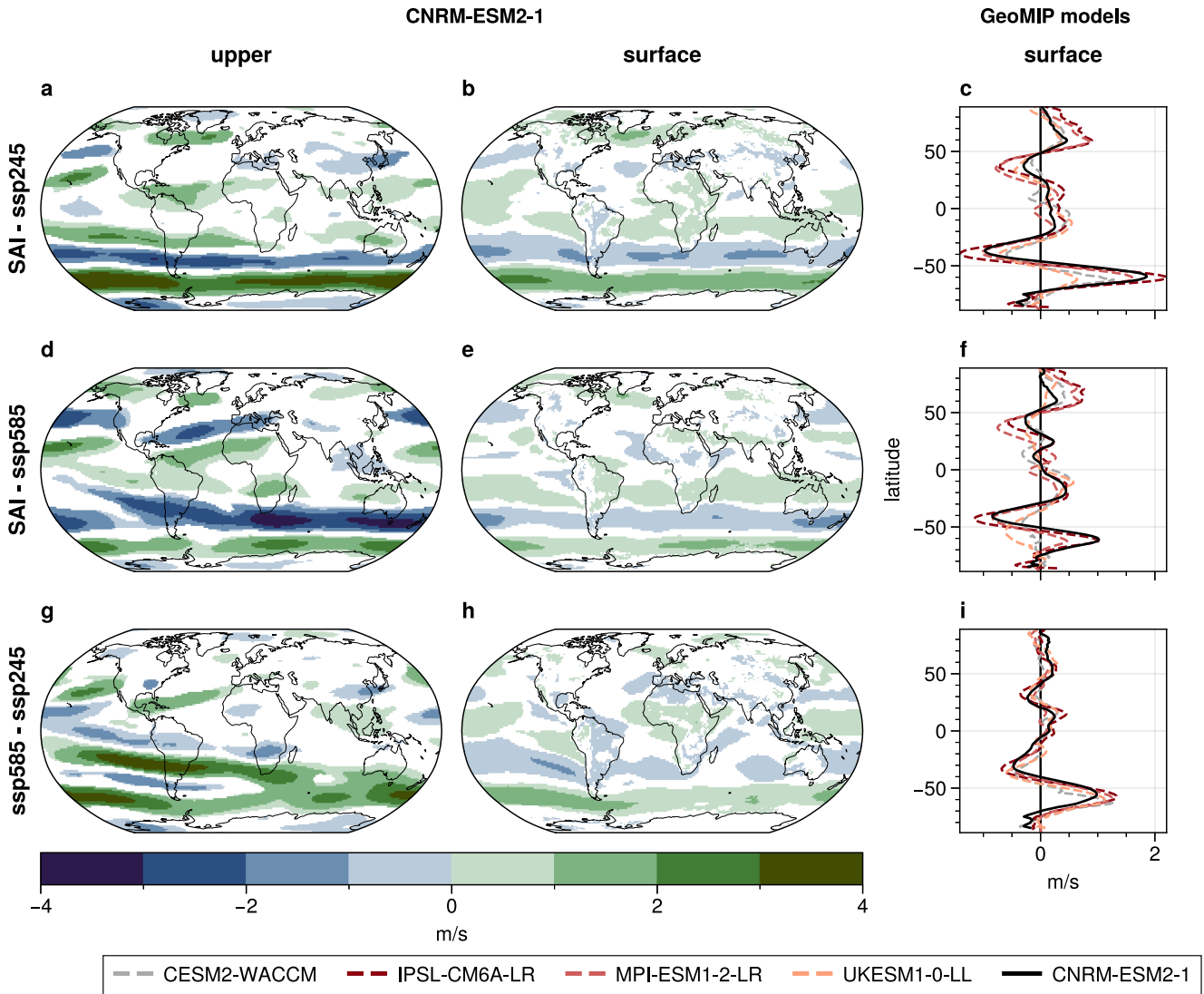
Figure 2. Difference in 2090–99 mean zonal winds between (a) and (c) SAI and SSP245, (d)–(f) SAI and SSP585 and (g)–(i) SSP245 and SSP585 in (a, d, g) the upper troposphere (200–400 hPa) and (b, c, e, f, h, i) at the surface (850–1,050 hPa). Maps are related to output from CNRM-ESM2-1 only; line plots (c, f, i) display zonal mean zonal winds for the models participating in GeoMIP, regridded to the CNRM-ESM2-1 resolution. Colored areas on the maps are statistically significant ($p < 0.05$).

(Figure 2) which are fairly consistent zonally across the different models participating in GeoMIP (Figures 2c, 2f, and 2i). Regardless of altitude or scenario-comparison, the largest differences are registered in the Southern Hemisphere (SH) for all models: Here, the westerlies' shift toward the pole is more pronounced under SAI compared to the SSP-scenarios and, comparing the SSP-scenarios, there is a more intense strengthening of the westerlies and poleward shift of the SH jet for SSP585 compared to SSP245 at the end of the century. The signal is strongest in the upper troposphere for all scenario-comparisons with differences in zonal wind speed of up to 5.2 (3.6–6.8) m/s and −4.0 (−4.9–−3.0) m/s for SAI-SSP245 and 5.0 (4.1–5.8) m/s and −2.6 (−3.3–−1.9) m/s for SAI-SSP585 (Figures 2a, 2 d, and 2g). While the sign of difference between SAI and the SSPs stays consistent across most seasons, the intensity varies (Figures S10 and S11 in Supporting Information S1).

In the NH, the changes are less latitudinally and, over the Atlantic Ocean, altitudinally consistent. While both upper tropospheric and surface winds show a pronounced equatorward shift of the midlatitude westerlies over the Pacific under SAI compared to the SSPs, the upper troposphere over the Atlantic entails a strengthened equatorward shift of the subtropical jet that does not propagate as much to the surface as for the SH (Figure 2, Figures
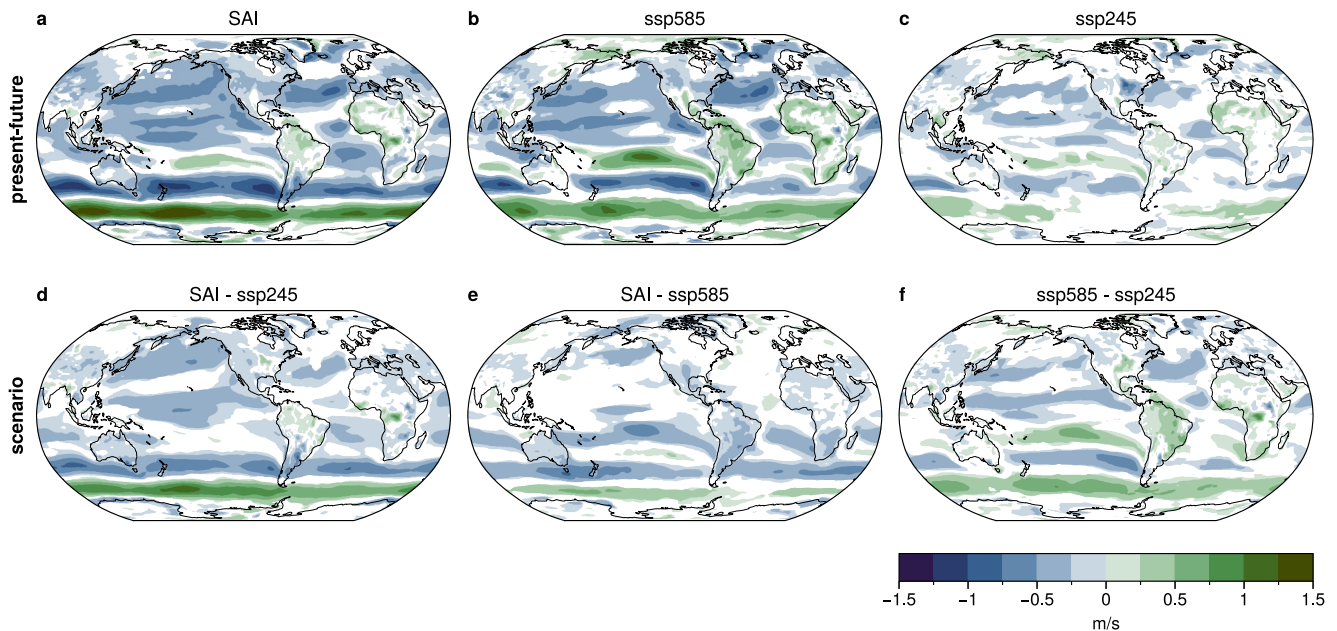
Figure 3. 150 m wind speed comparing present (2015–2024) and future (2090–2099) states under (a) SAI, (b) SSP585 and (c) SSP245 and comparing future states of scenarios (d) SAI and SSP245, (e) SAI and SSP585 and (f) SSP585 and SSP245. Colored areas are statistically significant ($p < 0.05$).

S9 and S12 in Supporting Information S1). The largest circulation changes occur in the upper troposphere and stratosphere (Figure 2, Figure S12 in Supporting Information S1).

Variation in large-scale circulation has been attributed to temperature changes in the stratosphere and resulting increases or decreases in the temperature gradients at the surface and/or the upper troposphere (Baldwin & Dunkerton, 2001; Charlesworth et al., 2023; DallaSanta et al., 2019; Graf, 1992; Simpson et al., 2019; Stenchikov et al., 2002). In our simulations we see a temperature shift of up to 7.3 (7.1–7.4; SSP245) K and 8.5 (8.2–8.8; SSP585) K under SAI compared to the SSP-scenarios in the tropical stratosphere at around 80 hPa (Figure S13 in Supporting Information S1), smaller than most other Earth System Models that have conducted the same experiments (Figure S15 in Supporting Information S1). As expected, temperatures at the surface are lower under SAI than SSP585, especially in the tropics, which is a common phenomenon observed in SRM simulations. Due to the augmented CO_2 concentration, which increases the rate that the stratosphere radiates heat to space, the stratosphere is colder under SSP585 than SSP245 (Figure S13c in Supporting Information S1).

Long-term average wind speed is substantially lower in the NH under SAI compared to the present (Figure 3a) and compared to the SSPs (Figures 3d and 3e). A trend fairly consistent throughout the scenarios but most noticeable in SSP585 is the increase in wind speed in tropical land regions compared to the present, especially in Brazil and on the African continent. Most other land regions experience reductions in wind speed (Figures 3a–3c).

For a comparison of zonal wind and temperature changes under SAI in CNRM-ESM2-1 versus other Earth System Models that have simulated the same scenarios as used in this study see Text S2 in Supporting Information S1 "Performance of CNRM-ESM2-1 in simulating zonal wind changes under SAI in context with other GeoMIP models."

3.2. SAI Effect on Onshore and Offshore Wind Potential

Results in this part are presented with respect to three different areas of interest: long-term relative seasonal changes, changes in extended low-energy periods (LEW) and the effect of changes in high hourly wind speed on annual energy production.

Figure 4 displays the relative difference in 2090–99 seasonal wind potential between the SSP-scenarios and SAI (see Figure S16 in Supporting Information S1 for 10-year mean present to future comparisons for each scenario). The sign of change is relatively consistent, although varying in strength, through the different seasons for SAI
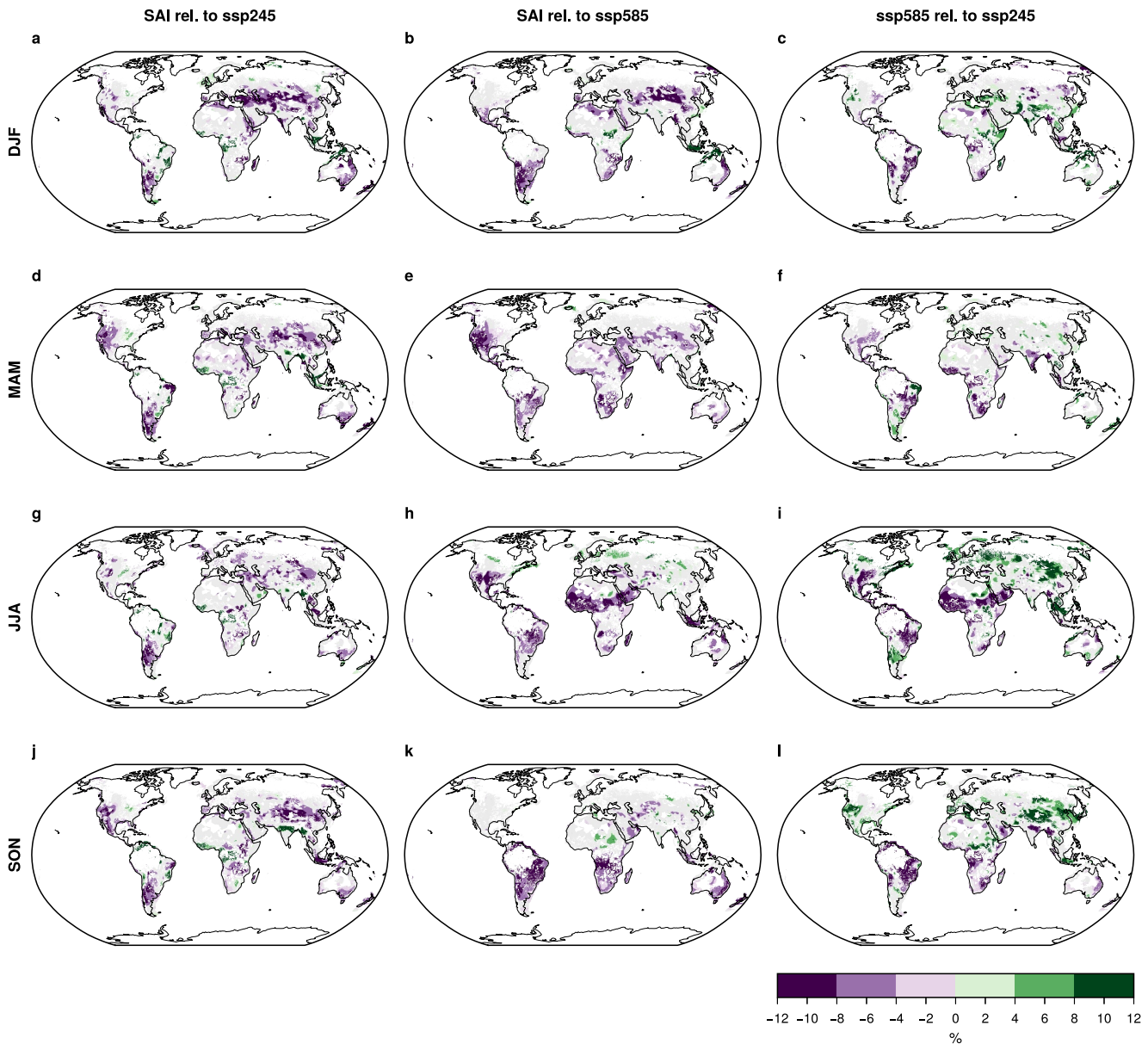
Figure 4. Relative differences in seasonal 2090–2099 wind potential for (a, d, g, j) SSP245 to SAI, (b, e, h, k) for SSP585 to SAI and (c, f, i, l) for SSP245 to SSP585 in the seasons (a)–(c) December, January, February (DJF), (d)–(f) March, April, Mai (MAM), (g)–(i) June, July, August (JJA) and (j–l) September, October, November (SON). Colored areas are statistically significant $p < 0.05$, gray areas are considered suitable for wind production but show no significant change. *x* rel. to *y* denotes (*x*–*y*)/*y*.

relative to SSP245, except for the South East Asian and Northern European region, where DJF and MAM show a large increase in wind potential, while JJA and SON show a decrease (Figures 4a, 4 d, 4g, and 4j). The same seasonal pattern is visible for SAI relative to SSP585 in South East Asia, but not in Europe. In general, the seasons show a less consistent signal between SSP585 and SAI than for SSP245 and SAI. For example, apart from Europe and South East Asia, also Central Africa and Central Asia show different trends depending on the season when comparing SSP585 with SAI (Figures 4b, 4 e, 4h, and 4k). While there is not one single region that stands out with especially large differences compared to others, the most pronounced differences in SSP585 to SAI are the large decrease in JJA in the southern Sahara (Figure 4h), the decrease in northern China in DJF (Figure 4b), the decrease in South America through all seasons but especially in Brazil in SON (Figure 4k) and Argentina, Bolivia and Paraguay in DJF (Figure 4b) and the increase in South East Asia and the Chad and Sudan area in the south-east of the Sahara desert in DJF (Figure 4b). For SSP245 to SAI, Central Asia sees a significant decrease through all
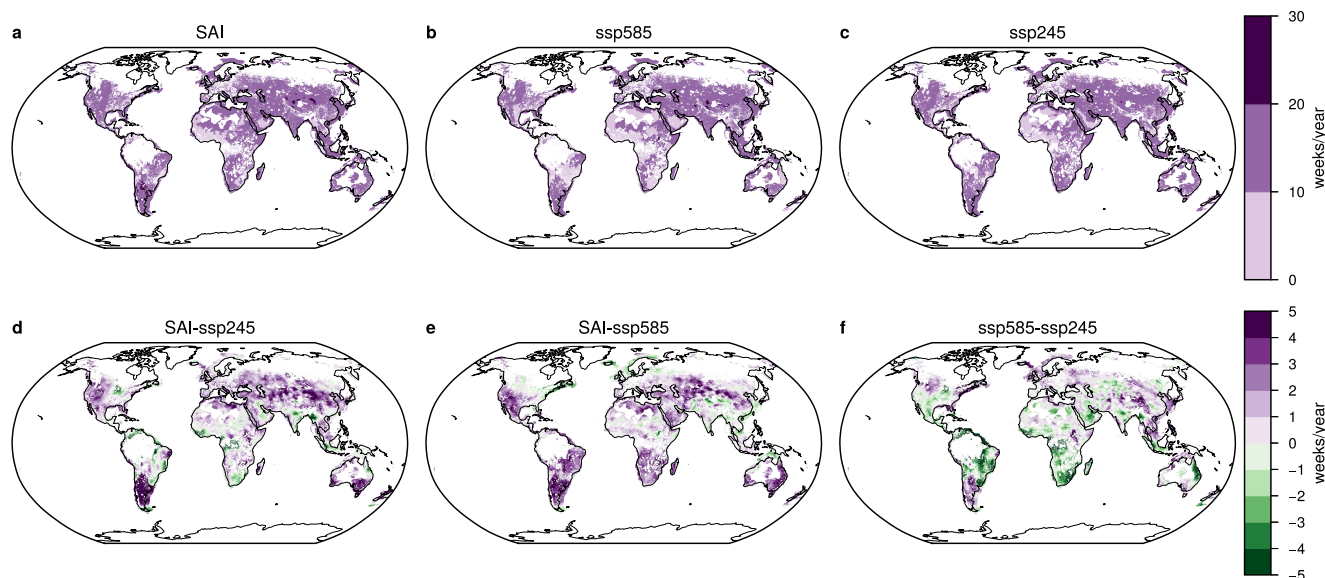
Figure 5. Low Energy Week (LEW) metric for (a) SAI, (b) SSP585 and (c) SSP245. The LEW is calculated between the present (2015–2019) and the future (2095–2099). See Baur et al. (2024) for the LEW equation. (d)–(f) are the differences between (a) and (c).

seasons but especially in DJF (Figure 4a). DJF furthermore indicates a large increase for southern South East Asia, northern offshore Australia and Central and South-East Brazil (Figure 4a). In MAM, East Brazil shows a big decreasing signal (Figure 4d). The SON months see a large increase in potential under SAI for Myanmar and Central/North India (Figure 4j). While the regional differences are diverse and large frequently reaching 12%, globally integrated relative differences are modest. SAI potential is 3.3 (2.9–3.7) % lower onshore and 2.6 (2.2–3.1) % lower offshore than for SSP245 and 4.6 (4.2–5.0) % lower onshore and 2.3 (2.0–2.6) % lower offshore than for SSP585. Between the conventional SSP-scenarios, there is no difference in potential since the 0.6 (0.0–1.2) % reduction in offshore potential under SSP585 compared to SSP245 is offset by the 0.6 (0.0–1.1) % increase in onshore potential.

The LEW metric assesses which regions experience prolonged periods of particularly low energy production. Figure 5 displays the number of weeks per year in SAI, SSP585 and SSP245 that have a wind energy output below the current (2015–2024) 20th seasonal percentile. Areas with up to 10 weeks per year imply that they stay unchanged in terms of low energy weeks or have less than in the present. Globally, most areas see an increase of 10–20 weeks per year in LEWs regardless of the scenario. West Africa, parts of the Arabian Peninsula and south-east Brazil see no change or a decrease in LEWs in all scenarios. When comparing the scenarios with each other and refining the color-coding, substantial differences become apparent (Figures 5d–5f). SAI leads to an increase of more than five additional LEWs per year compared to SSP245 or SSP585 in large parts of southern South America, south-east Australia, Central Asia and the Middle East. At the same time, many regions see less LEWs with SAI than with the SSP-scenarios. For example, compared to SSP245, the Great Plains in the US, several areas in Brazil, South Africa, West Africa, parts of the Arabian Peninsula, Myanmar and India and north-east Australia seem to benefit from SAI in terms of LEW count. Compared to SSP585, SAI appears to be especially advantageous in the north-east of North-America, northern Europe, the Arafura and Timor Sea between Australia and Indonesia/Timor and some regions in central China.

With some exceptions, such as north-east Australia, South Africa, northern Russia, offshore north-east North America and offshore Indonesia, the sign and magnitude of change stays consistent with the LEWs and the 10-year averages for SAI compared to SSP245 (Figure 5d, Figure S17a in Supporting Information S1). Similar for SAI versus SSP585, where exceptions are in the offshore area of north-east North-America, Mexico and southern US, offshore Borneo, Myanmar and South America, especially Argentina (Figure 5e, Figure S17b in Supporting Information S1).

To evaluate how much of the changes in wind potential are caused by changes in fast wind speed, we measure the annual power loss resulting from winds exceeding the cut-out threshold. Figure 6 shows which areas are mostly
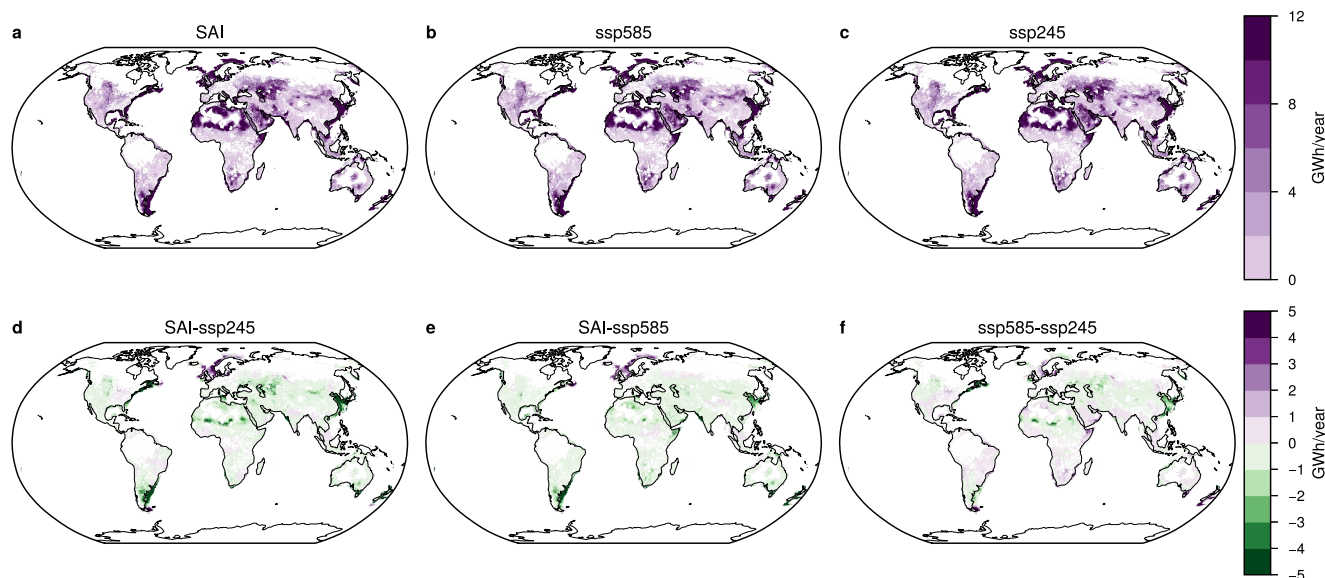
Figure 6. Difference between normal power curve setting and "no-cut-out" power curve setting for (a) SAI, (b) SSP245 and (c) SSP585. Differences in energy lost due to fast winds between (a) SAI and SSP245, (b) SAI and SSP585 and (c) SSP585 and SSP245.

affected by energy losses due to upper end winds in GWh per year per grid cell. Unsurprisingly, offshore areas are mostly affected by losses due to fast winds since wind is generally slower over land areas (Figures 6a–6c) and we applied lower suitability restrictions on offshore than onshore grid cells. Nevertheless, there are several onshore areas that see substantial reductions, such as the Great Plains in the US, the Southern parts of the Sahara, Central Asia and Russia. The differences between the scenarios are displayed in Figures 6d–6f. Offshore northern Europe, the tip of Argentina and eastern Canada are the only regions that have substantially higher losses due to fast winds under SAI than the SSP-scenarios. SAI makes winds offshore of China, eastern USA, New Zealand and southeast South America and, onshore, the Sahara more accessible to energy generation. The total global energy loss due to fast winds is lowest for SAI with 8.5 (8.3–8.7) PWh/yr (2.6%) and identical for SSP245 and SSP585 with 8.9 (8.8–9.0) PWh/yr (2.7%).

4. Discussion

In this study, we examined the interplay between Stratospheric Aerosol Injections (SAI) and renewable wind energy potential. We found large regional changes in wind potential under SAI compared to a medium emission (SSP245) or very high emission (SSP585) climate state depending on the season and region (Figures 4 and 5). The change in potential under SAI is regionally highly diverse with magnitudes frequently reaching 12% and more. These large regional differences average out to a total global potential that is slightly smaller than for SSP245 or SSP585.

Wind energy potential is highly dependent on wind resources and long-term changes therein are mainly due to large-scale atmospheric circulation (Jung & Schindler, 2022). Previous analyses on stratospheric aerosols and atmospheric circulation have found impacts on global and regional circulation patterns, in particular a poleward shift of the jet (Barnes et al., 2016; McCusker et al., 2014; Polvani & Kushner, 2002; Simpson et al., 2009, 2019). In our analysis, we also found significant differences in zonal wind between SAI and the SSP-scenarios, as well as under the SSP-scenarios themselves (Figure 2, Figure S12 in Supporting Information S1). The largest disparities exist within the Southern Hemisphere (SH) westerlies, which show a poleward shift under SAI compared to the SSP-scenarios, leading to both an increase and a decrease in the zonal mean wind (Figure 2, Figure S12 in Supporting Information S1). Our results are in agreement with those of Simpson et al. (2019), who studied alterations in large-scale circulation patterns using an SAI-setup known as GLENS. GLENS uses SAI to stay at 2020 conditions under an SSP585 baseline (Tilmes, Richter, Kravitz, et al., 2018). Simpson et al. (2019) conducted separate isolated forcing experiments to analyze how shifts in zonal wind patterns are driven by the stratospheric temperature change from SAI in GLENS. The authors note westerly stratospheric anomalies in the

extra-tropics of similar magnitude and pattern as those identified in our study, and attribute the dominant role driving this change in the SH to the heating of the tropical lower stratosphere, an effect likewise observed in our experiments (Figure S13 in Supporting Information S1). Studies on stratospheric aerosols from volcanic eruptions and circulation anomalies have made the same observation (Barnes et al., 2016; DallaSanta et al., 2019; Graft et al., 1993; Karpechko et al., 2010; Kirchner et al., 1999; McGraw et al., 2016) and attribution to stratospheric heating (Barnes et al., 2016; DallaSanta et al., 2019; Polvani & Kushner, 2002; Simpson et al., 2009). However, not all volcanic modeling results lead to the same conclusion: In the Northern Hemisphere (NH), Ramachandran et al. (2000) and Marshall et al. (2009) find an equatorward shift in response to the volcanic forcing instead and in the SH Robock et al. (2007) and Roscoe and Haigh (2007) found no or a slight equatorward shift. Volcanic modeling results, while a potential initial indication for SAI effects, are not entirely comparable to sustained and homogeneously spread aerosol injections that an idealized SAI deployment would consist of. Both Simpson et al. (2019) and McCusker et al. (2015) observe, and our study confirms, that the SH shows a much stronger signal, and that not all the changes in the NH are attributable to the stratospheric heating, such as, for example, in the North Pacific or the Atlantic during JJA (Simpson et al., 2019).

Tang et al. (2023) noted a total global reduction in onshore surface wind speed as a side effect of SAI using the same underlying scenarios as this study, but a different model (CESM2) and a lower temporal resolution. CESM2 differs from CNRM-ESM2-1 in the way that SAI is represented: While the modeling setup in this study uses scaled AOD to represent the stratospheric aerosols, CESM2 models equatorial SO_2 injections at an altitude of 25 km (Danabasoglu et al., 2020). Nevertheless, we see similar spatial patterns and magnitudes of change in surface wind speed as they do (Figures 5l–5k in Tang et al., 2023), especially over land (Figure 3e), and results from regional analyses also broadly overlap with our findings (Da-Allada et al., 2020; Mousavi et al., 2023). Da-Allada et al. (2020) and Mousavi et al. (2023) use data from the GLENS project (Tilmes, Richter, Kravitz, et al., 2018), which is simulated by the CESM1 model. GLENS provides a 20-member ensemble of a scenario using SAI to hold warming to a global average of 1.5°C from the same background conditions as in our study (SSP585). SAI is represented by SO_2 injections at 30°N, 30°S, 15°N, and 15°S, which are annually adjusted by a feedback-control algorithm. However, Xie et al. (2022) used a 6-model ensemble to identify the impacts of SAI on the Atlantic Meridional Overturning Circulation and report changes in global wind speed patterns as a result of SAI that are different from ours. They use the GeoMIP experiment G4 (Kravitz et al., 2013), which corresponds to a SSP245 background with a constant amount of equatorial SAI during 50 years. The divergence in results from Xie et al. (2022) and this paper may be partially explained by the difference in scenario comparisons but it nevertheless suggests that the impacts of SAI on wind are not well understood to date. The scenario-comparisons in Figures 2 and 3 suggest that SAI does not fully compensate for changes from global warming but modifies wind resources in a novel way.

While no studies exist to date that evaluate wind energy potential changes under SRM, studies looking at changes in WRE potential due to climate change have found regionally highly diverse trends (e.g., Gernaat et al., 2021; Solaun & Cerdá, 2019; Tobin et al., 2015). We generally see similar developments for the SSP245 and SSP585 comparison as other studies that look at wind potential under climate change. Remarkable similarities exist on the South American (De Jong et al., 2019; Gernaat et al., 2021; Pereira De Lucena et al., 2010; Pereira et al., 2013) and African continent (Gernaat et al., 2021; Sawadogo et al., 2021) and Europe (Carvalho et al., 2017; Davy et al., 2018; Gernaat et al., 2021; Tobin et al., 2015, 2018). The trend of increased wind energy in some northern European areas and lower wind energy in southern Europe and over Iceland can be explained with the tendency in Earth System Models to project more positive North Atlantic Oscillation (NAO) phases in a warmer future, a northward expansion of the Hadley cell, and a poleward shift of the jet stream and North Atlantic storm tracks (Carvalho et al., 2017; Pryor & Barthelmie, 2010; Tobin et al., 2015). In general, over Europe, the gradient of change in sea level pressure appears to be a good predictor of wind energy changes, where lower pressure is associated with increases in wind power and higher pressure with decreases (Tobin et al., 2015).

Gernaat et al. (2021) note a relative global reduction in offshore wind potential of 2.1% from historical (1970–2000) values to the end of the century under an RCP6.0 pathway using output from four climate models and a reduction in onshore potential by 4.1%. This is much higher than what we see for SSP245 versus SSP585, which has a global mean increase in onshore wind potential of 0.6 (0.0–1.1) % and a reduction in offshore potential of 0.6 (0.0–1.2) %. The comparison of our analyses is limited due to differences in underlying data and methodology and because our pathways result in a greater level of warming at the point of comparison (SSP585 vs. RCP6.0). However, the absolute temperature difference between SSP245 and SSP585 and Gernaat et al.'s (2021) historical

and end-of-century RCP6.0 value is of similar range. It is important to note that we compare scenarios of different warming at the same time, while Gernaat et al. (2021) used output from two different points in time. Despite the much smaller relative global change in potential with climate change compared to Gernaat et al.'s (2021) study, we calculate a total global potential that is broadly comparable with the results from Gernaat et al. (2021) and other studies that provide wind technical potential in energy units (Table S5 in Supporting Information S1; Archer & Jacobson, 2005; Bosch et al., 2017; Chu & Hawkes, 2020; Eurek et al., 2017; Gernaat et al., 2021; Hoogwijk, 2004; Krewitt et al., 2009; Lu et al., 2009; de Vries et al., 2007). Discrepancies are possible due to differences in the underlying models, unlike methodological approaches in calculating the potential, such as dissimilar assumptions regarding land suitability and the characteristics of the wind turbines, as well as the temporal resolution of the wind data. Contrary to those studies, our offshore potential is much greater than onshore, and energy losses offshore are also much higher than onshore (Figure 6). This is due to the stronger suitability constraints we apply on land grid cells and, as demonstrated by Martinez and Iglesias (2024) and Tian et al. (2019), the generally higher energy density offshore.

The LEW metric assesses whether an area encounters notably low weekly energy production variations, tackling the intermittency apprehension of renewable energy. Extended durations of considerably low production, as measured by the LEW metric, may be more impactful than a minor decline in mean production, as indicated by long-term average data. Several areas all over the globe see up to six additional or six fewer LEWs per year on average under SAI than the SSP-scenarios (Figure 5). The regional sign and magnitude of change mostly overlaps with that from the 10-year average changes (Figure S17 in Supporting Information S1). Baur et al. (2024) computed the LEW metric for Photovoltaic potential under SAI and found much larger increases in the order of up to 12 additional LEWs per year under SAI compared to SSP245 and less agreement on the sign and magnitude of change between long-term average and LEW difference. While their change in LEWs is much higher than what we see for wind, their relative decrease in long-term averages is much lower. This means that in those weeks where energy production is low for WRE, it is particularly low (low enough to count as a LEW), pulling the long-term average to higher numbers even though the total number of LEWs is lower than for solar renewable energy; whereas for Photovoltaic potential, the LEWs are frequent but not as unproductive. Since long periods of calm winds or cloudy conditions can be problematic for energy systems that rely on wind or solar renewable energy, it is relevant to look at whether regions with high general wind potential and high LEW increase correlate with regions of high solar potential and high solar LEW increase or trends in other types of intermittent renewable energies.

Panels a, b and c in Figure 6 demonstrate how large amounts of energy are lost due to faster than turbine cut-out-threshold wind velocities, especially offshore and over the Sahara. Wind turbines automatically shut off at a given wind speed threshold to protect themselves from damage (Saint-Drenan et al., 2020; Wood & Wollenberg, 1996). SAI, by leading to a slowing of winds in many for wind farms suitable regions, leads to less energy lost in WRE due to fast winds compared to SSP245 and SSP585 (Figures 6d and 6e), except over northern European offshore regions and at the tip of the South American continent, where SAI substantially increases long-term mean wind velocity (Figures 3d and 3e). The energy "gained" by the slowing of winds under SAI may be partially offset by the energy lost due to winds below the cut-in wind speed. However, due to the shape of the wind turbine power curve and as demonstrated by Saint-Drenan et al. (2020), the cut-out threshold has a much larger effect on total wind power production than the cut-in threshold and therefore the energy lost due to slower winds would be much lower.

Wind turbine energy output does not scale linearly with wind speed. Rather, they have a specific range of wind speeds in which they can produce electricity, described by the wind turbine power curve. Hence, lower (higher) wind speeds do not necessarily imply lower (higher) wind potential. Nevertheless, in our analysis, with the same time periods considered, the maps of differences in wind potential (Figure S16 in Supporting Information S1) correlate well (correlation coefficient 0.68 for SAI; 0.70 for the SSP-scenarios) with the maps of differences in wind speed (Figure 3). However, while total global potential is smaller under SAI than in the SSP-scenarios, SAI reduces the amount of energy that is lost due to fast winds that are not harvested by wind turbines (Figure 6). The observed decrease in WRE potential under SAI can therefore not be attributed to alterations in fast wind patterns and the current quest for wind turbines with ever-higher cut-out thresholds might take up a lower priority in an SAI-modified world. The overall reduction in WRE under SAI may hence be explained by the general long-term average reduction in wind speed, which is beneficial for high velocity regions that frequently surpass the cut-out threshold but disadvantageous in areas where wind velocity is in the range of the turbine power curve where

slower wind speed implies lower energy production. The total amount of energy lost due to fast winds for all three scenarios in our results is likely to be smaller than real-world applications would suggest, partly due to the Weibull distribution we apply to power output to represent variations in wind speed over time and space. This distribution results in power outputs for 1-hr average wind speeds that are above the cut-out wind speed (Figure S6 in Supporting Information S1), because even if the average wind speed is above the cut-out threshold, some samples of the Weibull distribution of that average wind speed may be below the cut-out and therefore produce electricity. In reality, however, the wind turbines are not instantly turned on and off for wind gusts above or below the cut-out threshold. This means that we could be overestimating the energy gained and underestimating the energy lost from fast winds. However, the wind turbine power curve represents the power output of a single turbine, and our positively skewed normal distribution of power output may be a better representation of the output from an entire grid cell, as other studies have shown (Bosch et al., 2017; Pryor & Barthelmie, 2010). In this study we did not consider directional changes in wind due to SAI. Given the substantial impact of wind speed fluctuations on power output and the lack of current modeling tools to robustly examine wind direction alterations (Arent et al., 2014; Pryor & Barthelmie, 2010; Solaun & Cerdá, 2019), the majority of existing studies have concentrated on investigating wind speed changes rather than directional changes.

Wind varies greatly in space and time (Cradden et al., 2014; J. C. Y. Lee et al., 2018; Yan et al., 2020) and our hourly input data, which represents entire 1° grid cells, is not able to fully reflect that. We regridded our wind data using a bilinear method to match the spatial resolution of the land use data rather than conducting a costly statistical downscaling. The subgrid variation of wind speeds in space and time is thus represented implicitly by the Weibull distribution. A constant Weibull shape parameter was used across the globe to ensure computational practicality. However, this approach may lead to under- or overestimation of wind power output in certain regions (Zhou & Smith, 2013). Selecting a constant shape parameter in the Weibull distribution is a simplification because it ultimately relies on the regional wind system and terrain. Nevertheless, any errors that may be produced from this simplification will affect all three scenarios equally and will be largely negated when comparing the scenarios. Our study focuses on the impact of SAI on wind renewable energy potential, specifically differences in predicted future states rather than precise and accurate regional representations of wind potential.

The study's findings are specific to a single SAI experimental set-up (continuous injection of sulfate aerosols) and model that may have a larger SAI signal than is currently considered in a hypothetical deployment scenario but allows us a larger signal-to-noise ratio. Since no other modeling groups have performed SAI experiments with hourly wind output, the study's robustness is constrained by these limitations and parallel modeling studies using additional Earth System Models would be highly valuable in assessing the robustness of signals. Until high temporal output is available from other modeling groups, the comparison of longer term output allows the contextualization of the results in this single-model study with potential changes had other models been used. In terms of zonal wind, CNRM-ESM2-1 performs better than the majority of Earth System Models of its generation (Figure S2 in Supporting Information S1) and long-term zonal wind trends are in line with other GeoMIP models (Figures 2c, 2f, and 2i; Text S2, Figure S14 in Supporting Information S1) and other studies looking at surface wind speed pattern changes under SAI (Da-Allada et al., 2020; Mousavi et al., 2023; Tang et al., 2023). CNRM-ESM2-1 is in the lower end of zonal wind changes from SAI compared to the other models in GeoMIP in the NH and in the upper end for changes in the SH. However, most areas with large changes in the SH are not included in the WRE calculation as they are not considered suitable. This implies that if output from other GeoMIP models had been included, changes in WRE potentials may have been more drastic. However, as our analysis shows (Figure 3, Figure S17 in Supporting Information S1), WRE changes are not fully predictable by changes in mean circulation and high frequency output is necessary to answer these questions properly. Therefore, to increase the robustness of the results, more model intercomparison studies such as Xie et al.'s (2022) study will need to be performed including those with interactive aerosol injection calculations instead of prescribed aerosols optical depth (Table S4 in Supporting Information S1), as well as different SAI experiment designs.

Not all regions have signal-to-noise ratios that are above 1 (Figure S16 in Supporting Information S1) or show statistically significant differences between scenarios (Figure 4, Figure S17 in Supporting Information S1), which is a common occurrence for low signal-to-noise variables such as wind. Despite the ongoing debate surrounding the consistency of Global Circulation Models with observations and their ability to simulate long-term trends (Pryor & Barthelmie, 2010; Pryor et al., 2020; Sheperd, 2014; Tian et al., 2019), particularly in coastal areas (Soares et al., 2017; Solaun & Cerdá, 2019), they are presently the most reliable source for global wind projections with SAI.

Our offshore energy assessment may further incur inaccuracies as a result of overestimating suitable areas by ignoring common shipping lanes and their unsuitability for wind farms. It is likely that for energy generation purposes unsuitable areas such as ports and frequently used transportation routes are located in proximity to areas that we consider particularly suitable, that is, areas close to population centers.

This study looks at the large-scale changes in the dynamics of the circulation system. While these have an important influence on local wind conditions, wind speeds in the lower levels of the atmospheric boundary layer, that is, those accessible to wind turbines, are highly susceptible to turbulence from small-scale features such as buildings, trees and valleys (Veers et al., 2019). These microscale processes are not resolved in our global analysis. An SSP245-world would likely have substantial differences in terms of land cover and population distribution compared to an SSP585- or an SAI-world. As these things are hard to predict and would complicate the comparison between scenarios, we chose equal area weighting for all scenarios. Nevertheless, future studies using higher resolution models or regional downscaling may improve the representation of these currently un-resolved smaller-scale processes.

Future research should not only consider other types of renewable energy sources such as biofuels and hydro-power but look at the effects of SAI on renewable energy sources in conjunction. This would allow to identify regions where not just one renewable energy technology, but potentially several, may experience a change in their productivity with SAI. Additionally, it is relevant to consider not only resource changes due to SRM but also demand changes. One could imagine a modified demand for heating and cooling under SRM, for example, Studies looking at other types of SRM, such as Marine Cloud Brightening, would offer a more complete picture on SRM and renewable energy. At the same time, improvements in the representation of SRM and the response of atmospheric circulation to a change in forcing in the Earth System Models would substantially increase accuracy of the results. Since stratospheric heating has been found to play an important role in changing large-scale circulation (Baldwin & Dunkerton, 2001; Charlesworth et al., 2023; DallaSanta et al., 2019; Graft et al., 1993; Simpson et al., 2019; Stenchikov et al., 2002), narrowing down the uncertainty related to the radiative properties of stratospheric aerosols could improve the understanding of the impacts of SAI on WRE. And lastly, since SAI seems to significantly affect the spatial distribution of wind resources, regional scale analyses are an essential addition in better understanding wind potential under SAI.

5. Conclusion

Wind renewable energy is considered a critical component in the efforts to reduce greenhouse gas emissions and transition to a more sustainable energy system. Studying the interplay between SAI and wind energy is important to understand whether mitigation and SAI could work together to address climate change. Here, we examined the alterations in wind patterns and renewable energy resources under SAI using the CNRM-ESM2-1.

We find that SAI, while counterbalancing the temperature increase of climate change, does not seem to fully counterbalance the effects of climate change on wind patterns and hence on WRE. Instead, our model simulations and long-term output from other GeoMIP models suggest that SAI may create new atmospheric circulation features which are not present in low- or high-warming futures (Figures 2 and 3, Figure S12 in Supporting Information S1). The overall long-term impact on WRE resources appears to be highly location-specific, with large increases and reductions in potential under SAI compared to SSP245 or SSP585 with magnitudes that frequently reach 12% (Figure 4, Figure S17 in Supporting Information S1). However, the long-term total global change in potential is a modest reduction compared with either conventional scenario. Perhaps more importantly, we find that SAI increases the number of weeks of considerably low production per year in most places around the world (Figure 5) compared to the SSP-scenarios and to the present, although to a much lesser degree than for solar renewable energy (Baur et al., 2024). We note that the reduction in long-term potential and the increase in low energy weeks are not due to an increase of wind speed under SAI but may rather be due to a general long-term average slowing of wind velocities (Figure 6).

This paper contributes to the ongoing discourse on climate intervention strategies and their implications for mitigation. Our findings underscore the importance of using model output with a high temporal resolution and a fairly large number of ensemble members to ensure a robust analysis of WRE changes. Future studies could additionally rely on higher spatial resolution models and a larger range of emission scenarios with SAI to test and improve accuracy of the current assumptions. Climate projections are still faced with the challenge of understanding the effect of global warming on atmospheric circulation change and pattern formation (Shepherd, 2014).

Improvements in these fundamental understandings might help in attributing the changes from the combined effects of global warming and SAI on wind allowing for a better investigation of the impacts of SAI on WRE potential. We suggest that further research is necessary to assess the wider impacts of SAI on renewable energies to enable more responsible and informed decision-making on climate intervention.

Conflict of Interest

The authors declare no conflicts of interest relevant to this study.

Data Availability Statement

The code and post-processed data is available at Baur (2024). The underlying data is output from the CNRM-ESM2-1 Earth System Model. Land use and land cover as well as population density projections are from the IMAGE3.0-LPJ model (Doelman et al., 2018; Stehfest et al., 2014). Land and ocean protected areas are from the International Union for Conservation of Nature (IUCN, 2023). The Exclusive Economic Zone (EEZ) is from the Flanders Marine Institute (2019), bathymetry and sea-ice information is output from the CNRM-ESM2-1 simulations. Figures were created using the matplotlib library and the matplotlib wrapper proplot.

References

Alizadeh, M. J., Kavianpour, M. R., Kamranzad, B., & Etemad-Shahidi, A. (2020). A distributed wind downscaling technique for wave climate modeling under future scenarios. *Ocean Modelling*, *145*, 101513. https://doi.org/10.1016/j.ocemod.2019.101513

Archer, C. L., & Jacobson, M. Z. (2005). Evaluation of global wind power. *Journal of Geophysical Research*, *110*(D12), 2004JD005462. https://doi.org/10.1029/2004JD005462

Arent, D. J., Sullivan, P., Heimiller, D., Lopez, A., Eurek, K., Badger, J., et al. (2012). *Improved offshore wind resource assessment in global climate stabilization scenarios*. National Renewable Energy Laboratory. NREL/TP-6A20–55049.

Arent, D. J., Tol, R. S. J., Faust, E., Hella, J. P., Kumar, S., Strzepek, K. M., et al. (2014). Key economic sectors and services. In C. B. Field, V. R. Barros, D. J. Dokken, K. J. Mach, M. D. Mastrandrea, T. E. Bilir, et al. (Eds.), *Climate Change 2014: Impacts, Adaptation, and Vulnerability. Part A: Global and Sectoral Aspects. Contribution of Working Group II to the Fifth Assessment Report of the Intergovernmental Panel on Climate Change* (pp. 659–708). Cambridge University Press.

Aukitino, T., Khan, M. G. M., & Ahmed, M. R. (2017). Wind energy resource assessment for Kiribati with a comparison of different methods of determining Weibull parameters. *Energy Conversion and Management*, *151*, 641–660. https://doi.org/10.1016/j.enconman.2017.09.027

Baldwin, M. P., & Dunkerton, T. J. (2001). In *Stratospheric harbingers of anomalous weather Regimes* (Vol. 294).

Barnes, E. A., Solomon, S., & Polvani, L. M. (2016). Robust wind and precipitation responses to the Mount Pinatubo eruption, as simulated in the CMIP5 models. *Journal of Climate*, *29*(13), 4763–4778. https://doi.org/10.1175/JCLI-D-15-0658.1

Baur, S. (2024). Data and code for journal article change in wind renewable energy potential under stratospheric aerosol injections [Dataset]. *Zenodo*. https://doi.org/10.5281/zenodo.10666778

Baur, S., Sanderson, B. M., Séférian, R., & Terray, L. (2024). Solar radiation modification challenges decarbonization with renewable solar energy. *Earth System Dynamics*, *15*(2), 307–322. https://doi.org/10.5194/esd-15-307-2024

Bosch, J., Staffell, I., & Hawkes, A. D. (2017). Temporally-explicit and spatially-resolved global onshore wind energy potentials. *Energy*, *131*, 207–217. https://doi.org/10.1016/j.energy.2017.05.052

Burton, T., Sharpe, D., Jenkins, N., & Bossanyi, E. (2001). *Wind energy handbook*. John Wiley & Sons. https://doi.org/10.1002/0470846062

Byers, E., Krey, V., Kriegler, E., Riahi, K., Schaeffer, R., Kikstra, J., et al. (2022). AR6 scenarios database [Dataset]. https://doi.org/10.5281/zenodo.7197970

Carrillo, C., Obando Montaño, A. F., Cidrás, J., & Díaz-Dorado, E. (2013). Review of power curve modelling for wind turbines. *Renewable and Sustainable Energy Reviews*, *21*, 572–581. https://doi.org/10.1016/j.rser.2013.01.012

Carvalho, D., Rocha, A., Gómez-Gesteira, M., & Silva Santos, C. (2017). Potential impacts of climate change on European wind energy resource under the CMIP5 future climate projections. *Renewable Energy*, *101*, 29–40. https://doi.org/10.1016/j.renene.2016.08.036

CAT (Climate Action Tracker). (2023). 2100 Warming Projections: Emissions and expected warming based on pledges and current policies. Retrieved from https://climateactiontracker.org/global/temperatures/

Chang, T.-J., Chen, C.-L., Tu, Y.-L., Yeh, H.-T., & Wu, Y.-T. (2015). Evaluation of the climate change impact on wind resources in Taiwan Strait. *Energy Conversion and Management*, *95*, 435–445. https://doi.org/10.1016/j.enconman.2015.02.033

Charlesworth, E., Plöger, F., Birner, T., Baikhadzhaev, R., Abalos, M., Abraham, N. L., et al. (2023). Stratospheric water vapor affecting atmospheric circulation. *Nature Communications*, *14*(1), 3925. https://doi.org/10.1038/s41467-023-39559-2

Cheng, W., MacMartin, D. G., Dagon, K., Kravitz, B., Tilmes, S., Richter, J. H., et al. (2019). Soil moisture and other hydrological changes in a stratospheric aerosol geoengineering large ensemble. *Journal of Geophysical Research: Atmospheres*, *124*(23), 12773–12793. https://doi.org/10.1029/2018JD030237

Chu, C.-T., & Hawkes, A. D. (2020). A geographic information system-based global variable renewable potential assessment using spatially resolved simulation. *Energy*, *193*, 116630. https://doi.org/10.1016/j.energy.2019.116630

Clarke, L., Wei, Y.-M., De La Vega Navarro, A., Garg, A., Hahmann, A. N., Khennas, S., et al. (2022). Energy systems. In P. R. Shukla, J. Skea, R. Slade, A. Al Khourdajie, R. van Diemen, D. McCollum, et al. (Eds.), *IPCC, 2022: Climate Change 2022: Mitigation of Climate Change. Contribution of Working Group III to the Sixth Assessment Report of the Intergovernmental Panel on Climate Change*. Cambridge University Press. https://doi.org/10.1017/9781009157926.008

Climate Overshoot Commission. (2023). *Reducing the risks of climate Overshoot*. Climate Overshoot Commission. Retrieved from https://www.overshootcommission.org/report

Cradden, L., Restuccia, F., Hawkins, S., & Harrison, G. (2014). Consideration of wind speed variability in creating a regional aggregate wind power time series. *Resources*, *3*(1), 215–234. https://doi.org/10.3390/resources3010215

Da-Allada, C. Y., Baloïtcha, E., Alamou, E. A., Awo, F. M., Bonou, F., Pomalegni, Y., et al. (2020). Changes in West African summer monsoon precipitation under stratospheric aerosol geoengineering. *Earth's Future*, *8*(7), e2020EF001595. https://doi.org/10.1029/2020EF001595

Dai, Z., Weisenstein, D. K., & Keith, D. W. (2018). Tailoring meridional and seasonal radiative forcing by sulfate aerosol solar geoengineering. *Geophysical Research Letters*, *45*(2), 1030–1039. https://doi.org/10.1002/2017GL076472

DallaSanta, K., Gerber, E. P., & Toohey, M. (2019). The circulation response to volcanic eruptions: The key roles of stratospheric warming and eddy interactions. *Journal of Climate*, *32*(4), 1101–1120. https://doi.org/10.1175/JCLI-D-18-0099.1

Danabasoglu, G., Lamarque, J.-F., Bacmeister, J., Bailey, D. A., DuVivier, A. K., Edwards, J., et al. (2020). The community Earth system model version 2 (CESM2). *Journal of Advances in Modeling Earth Systems*, *12*(2), e2019MS001916. https://doi.org/10.1029/2019MS001916

Davy, R., Gnatiuk, N., Pettersson, L., & Bobylev, L. (2018). Climate change impacts on wind energy potential in the European domain with a focus on the Black Sea. *Renewable and Sustainable Energy Reviews*, *81*, 1652–1659. https://doi.org/10.1016/j.rser.2017.05.253

De Jong, P., Barreto, T. B., Tanajura, C. A. S., Kouloukoui, D., Oliveira-Esquerre, K. P., Kiperstok, A., & Torres, E. A. (2019). Estimating the impact of climate change on wind and solar energy in Brazil using a South American regional climate model. *Renewable Energy*, *141*, 390–401. https://doi.org/10.1016/j.renene.2019.03.086

de Vries, B. J. M., van Vuuren, D. P., & Hoogwijk, M. M. (2007). Renewable energy sources: Their global potential for the first-half of the 21st century at a global level: An integrated approach. *Energy Policy*, *35*(4), 2590–2610. https://doi.org/10.1016/j.enpol.2006.09.002

Doelman, J. C., Stehfest, E., Tabeau, A., Van Meijl, H., Lassaletta, L., Gernaat, D. E. H. J., et al. (2018). Exploring SSP land-use dynamics using the IMAGE model: Regional and gridded scenarios of land-use change and land-based climate change mitigation [Software]. *Global Environmental Change*, *48*, 119–135. https://doi.org/10.1016/j.gloenvcha.2017.11.014

Dvorak, M. J., Archer, C. L., & Jacobson, M. Z. (2010). California offshore wind energy potential. *Renewable Energy*, *35*(6), 1244–1254. https://doi.org/10.1016/j.renene.2009.11.022

Elliot, D., & Schwartz, M. (1993). *Wind energy potential in the United States*. Pacific Northwest Laboratory.

Elsner, P. (2019). Continental-scale assessment of the African offshore wind energy potential: Spatial analysis of an under-appreciated renewable energy resource. *Renewable and Sustainable Energy Reviews*, *104*, 394–407. https://doi.org/10.1016/j.rser.2019.01.034

Eskin, N., Artar, H., & Tolun, S. (2008). Wind energy potential of Gökçeada Island in Turkey. *Renewable and Sustainable Energy Reviews*, *12*(3), 839–851. https://doi.org/10.1016/j.rser.2006.05.016

Eurek, K., Sullivan, P., Gleason, M., Hettinger, D., Heimiller, D., & Lopez, A. (2017). An improved global wind resource estimate for integrated assessment models. *Energy Economics*, *64*, 552–567. https://doi.org/10.1016/j.eneco.2016.11.015

Flanders Marine Institute. (2019). Maritime boundaries geodatabase: Maritime boundaries and exclusive economic zones (200NM), version 11 [Dataset]. Retrieved from https://www.marineregions.org/

Gernaat, D. E. H. J., de Boer, H. S., Daioglou, V., Yalew, S. G., Müller, C., & van Vuuren, D. P. (2021). Climate change impacts on renewable energy supply. *Nature Climate Change*, *11*(2), 119–125. https://doi.org/10.1038/s41558-020-00949-9

Graf, H.-F. (1992). Arctic radiation deficit and climate variability. *Climate Dynamics*, *7*(1), 19–28. https://doi.org/10.1007/BF00204818

Graft, H.-F., Kirchner, I., Robock, A., & Schult, I. (1993). Pinatubo eruption winter climate effects: Model versus observations. *Climate Dynamics*, *9*(2), 81–93. https://doi.org/10.1007/BF00210011

Hoogwijk, M. M. (2004). *On the global and regional potential of renewable energy sources = Over het mondiale en regionale potentieel van hernieuwbare energiebronnen*. Universiteit Utrecht, Faculteit Scheikunde.

Horton, J. B. (2015). The emergency framing of solar geoengineering: Time for a different approach. *The Anthropocene Review*, *2*(2), 147–151. https://doi.org/10.1177/2053019615579922

IPCC. (2018). Summary for policymakers. In V. Masson-Delmotte, P. Zhai, H.-O. Pörtner, D. Roberts, J. Skea, P.R. Shukla, et al. (Eds.), *Global Warming of 1.5°C. An IPCC Special Report on the impacts of global warming of 1.5°C above pre-industrial levels and related global greenhouse gas emission pathways, in the context of strengthening the global response to the threat of climate change, sustainable development, and efforts to eradicate poverty* (pp. 3–24). Cambridge University Press. https://doi.org/10.1017/9781009157940.001

IUCN (International Union for Conservation of Nature). (2023). The world database on protected areas (WDPA) [Dataset]. Retrieved from www.protectedplanet.net

Jung, C., & Schindler, D. (2022). A review of recent studies on wind resource projections under climate change. *Renewable and Sustainable Energy Reviews*, *165*, 112596. https://doi.org/10.1016/j.rser.2022.112596

Jung, C., Schindler, D., & Laible, J. (2018). National and global wind resource assessment under six wind turbine installation scenarios. *Energy Conversion and Management*, *156*, 403–415. https://doi.org/10.1016/j.enconman.2017.11.059

Justus, C. G., Hargraves, W. R., Mikhail, A., & Graber, D. (1978). Methods for estimating wind speed frequency distributions. *Journal of Applied Meteorology*, *17*(3), 350–353. https://doi.org/10.1175/1520-0450(1978)017<0350:mfewsf>2.0.co;2

Karpechko, A. Y., Gillett, N. P., Dall'Amico, M., & Gray, L. J. (2010). Southern hemisphere atmospheric circulation response to the El Chichón and Pinatubo eruptions in coupled climate models: Southern Hemisphere Response to El Chichón and Pinatubo. *Quarterly Journal of the Royal Meteorological Society*, *136*(652), 1813–1822. https://doi.org/10.1002/qj.683

Kirchner, I., Stenchikov, G. L., Graf, H.-F., Robock, A., & Antufia, J. C. (1999). Climate model simulation of winter warming and summer cooling following the 1991 Mount Pinatubo volcanic eruption. *Journal of Geophysical Research*, *104*(D16), 19039–19055. https://doi.org/10.1029/1999JD900213

Kravitz, B., Caldeira, K., Boucher, O., Robock, A., Rasch, P. J., Alterskjær, K., et al. (2013). Climate model response from the geoengineering model intercomparison project (GeoMIP). *Journal of Geophysical Research: Atmospheres*, *118*(15), 8320–8332. https://doi.org/10.1002/jgrd.50646

Kravitz, B., MacMartin, D. G., Tilmes, S., Richter, J. H., Mills, M. J., Cheng, W., et al. (2019). Comparing surface and stratospheric impacts of geoengineering with different SO_2 injection strategies. *Journal of Geophysical Research: Atmospheres*, *124*(14), 7900–7918. https://doi.org/10.1029/2019JD030329

Kravitz, B., MacMartin, D. G., Wang, H., & Rasch, P. J. (2016). Geoengineering as a design problem. *Earth System Dynamics*, *7*(2), 469–497. https://doi.org/10.5194/esd-7-469-2016

Kravitz, B., Robock, A., Tilmes, S., Boucher, O., English, J. M., Irvine, P. J., et al. (2015). The geoengineering model intercomparison project phase 6 (GeoMIP6): Simulation design and preliminary results. *Geoscientific Model Development*, *8*(10), 3379–3392. https://doi.org/10.5194/gmd-8-3379-2015

Krewitt, W., Nienhaus, K., Kleßmann, C., Capone, C., Stricker, E., Graus, W., et al. (2009). Role and potential of renewable energy and energy efficiency for global energy supply. *Climate Change*, *18*, 336. ISSN 1862-4359, Federal Environment Agency, Dessau-Roßlau, Germany.

Lee, H., Muri, H., Ekici, A., Tjiputra, J., & Schwinger, J. (2020). The response of terrestrial ecosystem carbon cycling under different aerosol-based radiation management geoengineering. *Earth System Dynamics*. https://doi.org/10.5194/esd-2020-57

Lee, J. C. Y., Fields, M. J., & Lundquist, J. K. (2018). Assessing variability of wind speed: Comparison and validation of 27 methodologies. *Wind Energy Science*, *3*(2), 845–868. https://doi.org/10.5194/wes-3-845-2018

Li, Y., Huang, X., Tee, K. F., Li, Q., & Wu, X.-P. (2020). Comparative study of onshore and offshore wind characteristics and wind energy potentials: A case study for southeast coastal region of China. *Sustainable Energy Technologies and Assessments*, *39*, 100711. https://doi.org/10.1016/j.seta.2020.100711

Liu, Z., Lang, X., Miao, J., & Jiang, D. (2023). Impact of stratospheric aerosol injection on the East Asian winter monsoon. *Geophysical Research Letters*, *50*(3), e2022GL102109. https://doi.org/10.1029/2022GL102109

Lu, X., McElroy, M. B., & Kiviluoma, J. (2009). Global potential for wind-generated electricity. *Proceedings of the National Academy of Sciences of the United States of America*, *106*(27), 10933–10939. https://doi.org/10.1073/pnas.0904101106

Lysen, E. H. (1983). *Introduction to wind energy*. CWD Publication. No. CWD 82–1.

Ma, J., Xie, S.-P., & Kosaka, Y. (2012). Mechanisms for tropical tropospheric circulation change in response to global warming. *Journal of Climate*, *25*(8), 2979–2994. https://doi.org/10.1175/JCLI-D-11-00048.1

MacCracken, M. C. (2009). On the possible use of geoengineering to moderate specific climate change impacts. *Environmental Research Letters*, *4*(4), 045107. https://doi.org/10.1088/1748-9326/4/4/045107

MacMartin, D. G., & Kravitz, B. (2019). The engineering of climate engineering. *Annual Review of Control, Robotics, and Autonomous Systems*, *2*(1), 445–467. https://doi.org/10.1146/annurev-control-053018-023725

Marshall, A. G., Scaife, A. A., & Ineson, S. (2009). Enhanced seasonal prediction of European winter warming following volcanic eruptions. *Journal of Climate*, *22*(23), 6168–6180. https://doi.org/10.1175/2009JCLI3145.1

Martinez, A., & Iglesias, G. (2024). Global wind energy resources decline under climate change. *Energy*, *288*, 129765. https://doi.org/10.1016/j.energy.2023.129765

McCusker, K. E., Armour, K. C., Bitz, C. M., & Battisti, D. S. (2014). Rapid and extensive warming following cessation of solar radiation management. *Environmental Research Letters*, *9*(2), 024005. https://doi.org/10.1088/1748-9326/9/2/024005

McCusker, K. E., Battisti, D. S., & Bitz, C. M. (2015). Inability of stratospheric sulfate aerosol injections to preserve the West Antarctic Ice Sheet. *Geophysical Research Letters*, *42*(12), 4989–4997. https://doi.org/10.1002/2015GL064314

McGraw, M. C., Barnes, E. A., & Deser, C. (2016). Reconciling the observed and modeled Southern Hemisphere circulation response to volcanic eruptions. *Geophysical Research Letters*, *43*(13), 7259–7266. https://doi.org/10.1002/2016GL069835

Mohammadi, K., Alavi, O., Mostafaeipour, A., Goudarzi, N., & Jalilvand, M. (2016). Assessing different parameters estimation methods of Weibull distribution to compute wind power density. *Energy Conversion and Management*, *108*, 322–335. https://doi.org/10.1016/j.enconman.2015.11.015

Mousavi, S. V., Karami, K., Tilmes, S., Muri, H., Xia, L., & Rezaei, A. (2023). Future dust concentration over the Middle East and North Africa region under global warming and stratospheric aerosol intervention scenarios. *Atmospheric Chemistry and Physics*, *23*(18), 10677–10695. https://doi.org/10.5194/acp-23-10677-2023

Müller-Hansen, F., Repke, T., Baum, C. M., Brutschin, E., Callaghan, M. W., Debnath, R., et al. (2023). Attention, sentiments and emotions towards emerging climate technologies on Twitter. *Global Environmental Change*, *83*, 102765. https://doi.org/10.1016/j.gloenvcha.2023.102765

O'Neill, B. C., Tebaldi, C., Van Vuuren, D. P., Eyring, V., Friedlingstein, P., Hurtt, G., et al. (2016). The scenario model intercomparison project (ScenarioMIP) for CMIP6. *Geoscientific Model Development*, *9*(9), 3461–3482. https://doi.org/10.5194/gmd-9-3461-2016

Pereira, E. B., Martins, F. R., Pes, M. P., Da Cruz Segundo, E. I., & Lyra, A. D. A. (2013). The impacts of global climate changes on the wind power density in Brazil. *Renewable Energy*, *49*, 107–110. https://doi.org/10.1016/j.renene.2012.01.053

Pereira De Lucena, A. F., Szklo, A. S., Schaeffer, R., & Dutra, R. M. (2010). The vulnerability of wind power to climate change in Brazil. *Renewable Energy*, *35*(5), 904–912. https://doi.org/10.1016/j.renene.2009.10.022

Perrin, O., Rootzén, H., & Taesler, R. (2006). A discussion of statistical methods used to estimate extreme wind speeds. *Theoretical and Applied Climatology*, *85*(3–4), 203–215. https://doi.org/10.1007/s00704-005-0187-3

Polvani, L. M., & Kushner, P. J. (2002). Tropospheric response to stratospheric perturbations in a relatively simple general circulation model. *Geophysical Research Letters*, *29*(7), 18-1–18-4. https://doi.org/10.1029/2001GL014284

Pryor, S. C., & Barthelmie, R. J. (2010). Climate change impacts on wind energy: A review. *Renewable and Sustainable Energy Reviews*, *14*(1), 430–437. https://doi.org/10.1016/j.rser.2009.07.028

Pryor, S. C., Barthelmie, R. J., Bukovsky, M. S., Leung, L. R., & Sakaguchi, K. (2020). Climate change impacts on wind power generation. *Nature Reviews Earth & Environment*, *1*(12), 627–643. https://doi.org/10.1038/s43017-020-0101-7

Ramachandran, S., Ramaswamy, V., Stenchikov, G. L., & Robock, A. (2000). Radiative impact of the Mount Pinatubo volcanic eruption: Lower stratospheric response. *Journal of Geophysical Research*, *105*(D19), 24409–24429. https://doi.org/10.1029/2000JD900355

Riahi, K., Schaeffer, R., Arango, J., Calvin, K., Guivarch, C., Hasegawa, T., et al. (2022). Mitigation pathways compatible with long-term goals. In P. R. Shukla, J. Skea, R. Slade, A. Al Khourdajie, R. van Diemen, D. McCollum, et al. (Eds.), *IPCC, 2022: Climate Change 2022: Mitigation of Climate Change. Contribution of Working Group III to the Sixth Assessment Report of the Intergovernmental Panel on Climate Change*. Cambridge University Press. https://doi.org/10.1017/9781009157926.005

Ripple, W. J., Wolf, C., Gregg, J. W., Rockström, J., Newsome, T. M., Law, B. E., et al. (2023). The 2023 state of the climate report: Entering uncharted territory. *BioScience*, *73*(12), 841–850. https://doi.org/10.1093/biosci/biad080

Robock, A., Adams, T., Moore, M., Oman, L., & Stenchikov, G. (2007). Southern Hemisphere atmospheric circulation effects of the 1991 Mount Pinatubo eruption. *Geophysical Research Letters*, *34*(23), 2007GL031403. https://doi.org/10.1029/2007GL031403

Robock, A., Oman, L., & Stenchikov, G. L. (2008). Regional climate responses to geoengineering with tropical and Arctic SO_2 injections. *Journal of Geophysical Research*, *113*(16), 1–15. https://doi.org/10.1029/2008JD010050

Roscoe, H. K., & Haigh, J. D. (2007). Influences of ozone depletion, the solar cycle and the QBO on the southern annular mode: Influences on the southern annular mode. *Quarterly Journal of the Royal Meteorological Society*, *133*(628), 1855–1864. https://doi.org/10.1002/qj.153

Royal Society. (2011). *Solar radiation management: The governance of research* (p. 70). The Royal Society of London. Retrieved from https://royalsociety.org/-/media/Royal_Society_Content/policy/projects/solar-radiation-governance/DES2391_SRMGI-report_web.pdf

Saint-Drenan, Y.-M., Besseau, R., Jansen, M., Staffell, I., Troccoli, A., Dubus, L., et al. (2020). A parametric model for wind turbine power curves incorporating environmental conditions. *Renewable Energy*, *157*, 754–768. https://doi.org/10.1016/j.renene.2020.04.123

Sawadogo, W., Reboita, M. S., Faye, A., da Rocha, R. P., Odoulami, R. C., Olusegun, C. F., et al. (2021). Current and future potential of solar and wind energy over Africa using the RegCM4 CORDEX-CORE ensemble. *Climate Dynamics*, *57*(5), 1647–1672. https://doi.org/10.1007/s00382-020-05377-1

Schäfer, S., Stelzer, H., Maas, A., & Lawrence, M. G. (2014). Earth's future in the Anthropocene: Technological interventions between piecemeal and utopian social engineering. *Earth's Future*, *2*(4), 239–243. https://doi.org/10.1002/2013EF000190

Séférian, R., Nabat, P., Michou, M., Saint-Martin, D., Voldoire, A., Colin, J., et al. (2019). Evaluation of CNRM Earth system model, CNRM-ESM2-1: Role of Earth system processes in present-day and future climate. *Journal of Advances in Modeling Earth Systems*, *11*(12), 4182–4227. https://doi.org/10.1029/2019MS001791

Shaw, T. A., Baldwin, M., Barnes, E. A., Caballero, R., Garfinkel, C. I., Hwang, Y.-T., et al. (2016). Storm track processes and the opposing influences of climate change. *Nature Geoscience*, *9*(9), 656–664. https://doi.org/10.1038/ngeo2783

Shepherd, T. (2014). Atmospheric circulation as a source of uncertainty in climate change projections. *Nature Geoscience*, *7*(10), 703–708. https://doi.org/10.1038/ngeo2253

Shi, H., Dong, Z., Xiao, N., & Huang, Q. (2021). Wind speed distributions used in wind energy assessment: A review. *Frontiers in Energy Research*, *9*. https://doi.org/10.3389/fenrg.2021.769920

Shin, J.-Y., Jeong, C., & Heo, J.-H. (2018). A novel statistical method to temporally downscale wind speed Weibull distribution using scaling property. *Energies*, *11*(3), 633. https://doi.org/10.3390/en11030633

Shu, Z. R., & Jesson, M. (2021). Estimation of Weibull parameters for wind energy analysis across the UK. *Journal of Renewable and Sustainable Energy*, *13*(2), 023303. https://doi.org/10.1063/5.0038001

Shu, Z. R., Li, Q. S., & Chan, P. W. (2015). Investigation of offshore wind energy potential in Hong Kong based on Weibull distribution function. *Applied Energy*, *156*, 362–373. https://doi.org/10.1016/j.apenergy.2015.07.027

Simpson, I. R., Blackburn, M., & Haigh, J. D. (2009). The role of eddies in driving the tropospheric response to stratospheric heating perturbations. *Journal of the Atmospheric Sciences*, *66*(5), 1347–1365. https://doi.org/10.1175/2008JAS2758.1

Simpson, I. R., Tilmes, S., Richter, J. H., Kravitz, B., MacMartin, D. G., Mills, M. J., et al. (2019). The regional hydroclimate response to stratospheric sulfate geoengineering and the role of stratospheric heating. *Journal of Geophysical Research: Atmospheres*, *124*(23), 12587–12616. https://doi.org/10.1029/2019JD031093

Soares, P. M. M., Lima, D. C. A., Cardoso, R. M., Nascimento, M. L., & Semedo, A. (2017). Western Iberian offshore wind resources: More or less in a global warming climate? *Applied Energy*, *203*, 72–90. https://doi.org/10.1016/j.apenergy.2017.06.004

Sohoni, V., Gupta, S. C., & Nema, R. K. (2016). A critical review on wind turbine power curve modelling techniques and their applications in wind based energy systems. *Journal of Energy*, *2016*, 1–18. https://doi.org/10.1155/2016/8519785

Solaun, K., & Cerdá, E. (2019). Climate change impacts on renewable energy generation. A review of quantitative projections. *Renewable and Sustainable Energy Reviews*, *116*, 109415. https://doi.org/10.1016/j.rser.2019.109415

Stehfest, E., Van Vuuren, D., Kram, T., Bouwman, L., Alkemade, R., Bakkenes, M., et al. (2014). *Integrated assessment of global environmental change with IMAGE 3.0. Model description and policy applications*. Netherlands Environmental Assessment Agency (The Hague).

Stenchikov, G., Robock, A., Ramaswamy, V., Schwarzkopf, M. D., Hamilton, K., & Ramachandran, S. (2002). Arctic Oscillation response to the 1991 Mount Pinatubo eruption: Effects of volcanic aerosols and ozone depletion. *Journal of Geophysical Research*, *107*(D24), ACL28-1–ACL28-16. https://doi.org/10.1029/2002JD002090

Tang, W., Tilmes, S., Lawrence, D. M., Li, F., He, C., Emmons, L. K., et al. (2023). Impact of solar geoengineering on wildfires in the 21st century in CESM2/WACCM6. *Atmospheric Chemistry and Physics*, *23*(9), 5467–5486. https://doi.org/10.5194/acp-23-5467-2023

Tian, Q., Huang, G., Hu, K., & Niyogi, D. (2019). Observed and global climate model based changes in wind power potential over the Northern Hemisphere during 1979–2016. *Energy*, *167*, 1224–1235. https://doi.org/10.1016/j.energy.2018.11.027

Tilmes, S., Mills, M. J., Niemeier, U., Schmidt, H., Robock, A., Kravitz, B., et al. (2015). A new Geoengineering Model Intercomparison Project (GeoMIP) experiment designed for climate and chemistry models. *Geoscientific Model Development*, *8*(1), 43–49. https://doi.org/10.5194/gmd-8-43-2015

Tilmes, S., Richter, J. H., Kravitz, B., Macmartin, D. G., Mills, M. J., Simpson, I. R., et al. (2018). CESM1(WACCM) stratospheric aerosol geoengineering large ensemble project. *Bulletin of the American Meteorological Society*, *99*(11), 2361–2371. https://doi.org/10.1175/BAMS-D-17-0267.1

Tilmes, S., Richter, J. H., Mills, M. J., Kravitz, B., MacMartin, D. G., Garcia, R. R., et al. (2018). Effects of different stratospheric SO_2 injection altitudes on stratospheric chemistry and dynamics. *Journal of Geophysical Research: Atmospheres*, *123*(9), 4654–4673. https://doi.org/10.1002/2017JD028146

Tilmes, S., Richter, J. H., Mills, M. J., Kravitz, B., MacMartin, D. G., Vitt, F., et al. (2017). Sensitivity of aerosol distribution and climate response to stratospheric SO_2 injection locations. *Journal of Geophysical Research: Atmospheres*, *122*(23), 12591–12615. https://doi.org/10.1002/2017JD026888

Tobin, I., Greuell, W., Jerez, S., Ludwig, F., Vautard, R., Van Vliet, M. T. H., & Bréon, F. M. (2018). Vulnerabilities and resilience of European power generation to 1.5°C, 2°C and 3°C warming. *Environmental Research Letters*, *13*(4), 044024. https://doi.org/10.1088/1748-9326/aab211

Tobin, I., Vautard, R., Balog, I., Bréon, F. M., Jerez, S., Ruti, P. M., et al. (2015). Assessing climate change impacts on European wind energy from ENSEMBLES high-resolution climate projections. *Climatic Change*, *128*(1–2), 99–112. https://doi.org/10.1007/s10584-014-1291-0

Tye, M. R., Stephenson, D. B., Holland, G. J., & Katz, R. W. (2014). A Weibull approach for improving climate model projections of tropical cyclone wind-speed distributions. *Journal of Climate*, *27*(16), 6119–6133. https://doi.org/10.1175/JCLI-D-14-00121.1

Valencia Ochoa, G., Núñez Alvarez, J., & Vanegas Chamorro, M. (2019). Data set on wind speed, wind direction and wind probability distributions in Puerto Bolivar - Colombia. *Data in Brief*, *27*, 104753. https://doi.org/10.1016/j.dib.2019.104753

Vautard, R., Cattiaux, J., Yiou, P., Thépaut, J.-N., & Ciais, P. (2010). Northern Hemisphere atmospheric stilling partly attributed to an increase in surface roughness. *Nature Geoscience*, *3*(11), 756–761. https://doi.org/10.1038/ngeo979

Veers, P., Dykes, K., Lantz, E., Barth, S., Bottasso, C. L., Carlson, O., et al. (2019). Grand challenges in the science of wind energy. *Science*, *366*(6464), eaau2027. https://doi.org/10.1126/science.aau2027

Veronesi, F., & Grassi, S. (2015). Comparison of hourly and daily wind speed observations for the computation of Weibull parameters and power output. In *2015 3rd International Renewable and Sustainable Energy Conference (IRSEC)* (pp. 1–6). Marrakech, Morocco: IEEE. https://doi.org/10.1109/IRSEC.2015.7455043

Wood, A. J., & Wollenberg, B. (1996). Power generation operation and control. In *Fuel and energy abstracts* (2nd ed., Vol. 37, p. 195). Elsevier.

Xie, M., Moore, J. C., Zhao, L., Wolovick, M., & Muri, H. (2022). Impacts of three types of solar geoengineering on the Atlantic meridional overturning circulation. *Atmospheric Chemistry and Physics*, *22*(7), 4581–4597. https://doi.org/10.5194/acp-22-4581-2022

Yan, B., Chan, P. W., Li, Q. S., He, Y. C., & Shu, Z. R. (2020). Characterising the fractal dimension of wind speed time series under different terrain conditions. *Journal of Wind Engineering and Industrial Aerodynamics*, *201*, 104165. https://doi.org/10.1016/j.jweia.2020.104165

Zeng, Z., Ziegler, A. D., Searchinger, T., Yang, L., Chen, A., Ju, K., et al. (2019). A reversal in global terrestrial stilling and its implications for wind energy production. *Nature Climate Change*, *9*(12), 979–985. https://doi.org/10.1038/s41558-019-0622-6

Zhou, Y., Luckow, P., Smith, S. J., & Clarke, L. (2012). Evaluation of global onshore wind energy potential and generation costs. *Environmental Science & Technology*, *46*(14), 7857–7864. https://doi.org/10.1021/es204706m

Zhou, Y., & Smith, S. J. (2013). Spatial and temporal patterns of global onshore wind speed distribution. *Environmental Research Letters*, *8*(3), 034029. https://doi.org/10.1088/1748-9326/8/3/034029

References From the Supporting Information

Boucher, O., Servonnat, J., Albright, A. L., Aumont, O., Balkanski, Y., Bastrikov, V., et al. (2020). Presentation and evaluation of the IPSL-CM6A-LR climate model. *Journal of Advances in Modeling Earth Systems*, *12*(7), e2019MS002010. https://doi.org/10.1029/2019MS002010

Eyring, V., Gillett, N. P., Achuta Rao, K. M., Barimalala, R., Barreiro Parrillo, M., Bellouin, N., et al. (2021). Human influence on the climate system. In V. Masson-Delmotte, P. Zhai, A. Pirani, S. L. Connors, C. Péan, S. Berger, et al. (Eds.), *Climate Change 2021: The Physical Science Basis. Contribution of Working Group I to the Sixth Assessment Report of the Intergovernmental Panel on Climate Change* (pp. 423–552). Cambridge University Press. https://doi.org/10.1017/9781009157896.005

Hersbach, H., Bell, B., Berrisford, P., Biavati, G., Horányi, A., Muñoz Sabater, J., et al. (2023). ERA5 monthly averaged data on single levels from 1940 to present. *Copernicus Climate Change Service (C3S) Climate Data Store (CDS)*. https://doi.org/10.24381/cds.f17050d7

Müller, W. A., Jungclaus, J. H., Mauritsen, T., Baehr, J., Bittner, M., Budich, R., et al. (2018). A higher-resolution version of the Max Planck Institute Earth system model (MPI-ESM1.2-HR). *Journal of Advances in Modeling Earth Systems*, *10*(7), 1383–1413. https://doi.org/10.1029/2017MS001217

Sellar, A. A., Jones, C. G., Mulcahy, J. P., Tang, Y., Yool, A., Wiltshire, A., et al. (2019). UKESM1: Description and evaluation of the U.K. Earth system model. *Journal of Advances in Modeling Earth Systems*, *11*(12), 4513–4558. https://doi.org/10.1029/2019MS001739

Vestas. (2023a). V236-15.0 MW™. Retrieved from https://www.vestas.com/en/products/offshore/V236-15MW

Vestas. (2023b). V162-6.2 MW™. Retrieved from https://www.vestas.com/en/products/enventus-platform/v162-6-2-mw

Visioni, D., MacMartin, D., Kravitz, B., Boucher, O., Jones, A., Lurton, T., et al. (2021). Identifying the sources of uncertainty in climate model simulations of solar radiation modification with the G6sulfur and G6solar Geoengineering Model Intercomparison Project (GeoMIP) simulations. *Atmospheric Chemistry and Physics*, 1–37. https://doi.org/10.5194/acp-2021-133